mmWave 6D Radio Localization With a Snapshot Observation From a Single BS

Mohammad A. Nazari, *Student Member, IEEE*, Gonzalo Seco-Granados, *Fellow, IEEE*, Pontus Johannisson, and Henk Wymeersch, *Senior Member, IEEE*

***Abstract*—Accurate and ubiquitous localization is crucial for a variety of applications such as logistics, navigation, intelligent transport, monitoring, control, and also for the benefit of communications. Exploiting millimeter-wave (mmWave) signals in 5G and Beyond 5G systems can provide accurate localization with limited infrastructure. We consider the single base station (BS) localization problem and extend it to 3D position and 3D orientation estimation of an unsynchronized multi-antenna user equipment (UE), using downlink multiple-input multiple-output orthogonal frequency-division multiplexing (MIMO-OFDM) signals. Through a Fisher information analysis, we show that the problem is often identifiable, provided that there is at least one multipath component in addition to the line-of-sight (LoS), even if the position of corresponding incidence point (IP) is a priori unknown. Subsequently, we pose a maximum likelihood (ML) estimation problem, to jointly estimate the 3D position and 3D orientation of the UE as well as several nuisance parameters (the UE clock offset and the positions of IPs corresponding to the multipath). The ML problem is a high-dimensional non-convex optimization problem over a product of Euclidean and non-Euclidean manifolds. To avoid complex exhaustive search procedures, we propose a geometric initial estimate of all parameters, which reduces the problem to a 1-dimensional search over a finite interval. Numerical results show the efficiency of the proposed ad-hoc estimation, whose gap to the Cramér-Rao bound (CRB) is tightened using the ML estimation.**

***Index Terms*—Localization, Orientation estimation, Mapping, Synchronization, Single anchor localization.**

I. Introduction

MMWAVE is the key enabling component of the fifth generation (5G) and beyond 5G (B5G) communication systems, which empowers the implementation of large antenna arrays for spatial multiplexing and provides massive bandwidths for high data rates [1]. Despite the favorable properties of mmWave, undesired effects, such as severe path loss and limited channel rank, challenge the technology to come up with advanced beamforming and resource allocation schemes [2]. To achieve this, information on the 3D location of mobile users can provide important side information, so that the BS can adjust its precoders to beam towards the UE [3]. Similarly, the UE can adjust its combiners, based on its 3D orientation, to maximize the received signal-to-noise ratio (SNR) [4]. While UE position estimation has been the main driver in 5G mmWave [5], there are many applications that need 6D information (3D position and 3D orientation, also known as the pose in robotics [6]): the position and heading of vehicles is needed in intelligent transport systems for driving assistance applications and platooning [7]; in assisted living facilities, the pose of residents is informative about their health status [8]; search-and-rescue operations involving UAVs require accurate and timely pose information for control, self-localization, and victim recovery [9]. Moreover, 6D localization is expected to be of importance in 6G, with applications such as augmented reality, robot interaction, and digital twins [10].

The source of this 6D information, whose estimation is referred to as *6D localization* in this paper, can be either external or internal to the communication systems. The external 6D localization systems can build on a mixed-technology solution, such as the combination of the global navigation satellite system (GNSS) (for 3D position) and inertial measurement unit (IMU) (for 3D orientation) [11]. However, such solutions can be inefficient in cost, complexity, or coverage. For example, GNSS might fail in indoor environments or urban canyons, while IMUs suffer from drifts and accumulative errors [12]. The alternative is to exploit the already deployed cellular communication infrastructure for 6D localization, and feed the 6D information to the communication system internally.

Prior to 5G, the majority of localization schemes in cellular networks relied on multiple synchronized base stations and time-difference-of-arrival (TDoA) measurements [13]. With the introduction of new dedicated positioning reference signals (PRSs) and measurements in 3GPP release 16 [14], a combination of angle and delay measurements has become possible [15]. Because of the high resolution in both temporal and angular domains, thanks to 400 MHz bandwidth at mmWave and large antenna arrays, respectively, multipath components can be better resolved [16], leading to new positioning architectures.

Manuscript received 6 April 2022; revised 30 November 2022; accepted 18 January 2023. Date of publication 17 February 2023; date of current version 18 July 2023. This work was supported in part by the Wallenberg AI, Autonomous Systems and Software Program (WASP), in part by the Swedish Research Council under Grant 2018-03701, in part by the European Commission through the H2020 Project Hexa-X under Grant 101015956, in part by the Spanish Research Agency under Project PID2020-118984GB-I00, and in part by the ICREA Academia Programme. The review of this article was coordinated by Prof. Zhu Han. *(Corresponding author: Mohammad A. Nazari.)*

Mohammad A. Nazari and Henk Wymeersch are with the Department of Electrical Engineering, Chalmers University of Technology, 41258 Göteborg, Sweden (e-mail: mohammad.nazari@chalmers.se; henkw@chalmers.se).

Gonzalo Seco-Granados is with the Department of Telecommunications and Systems Engineering, Universitat Autonoma de Barcelona, 08193 Barcelona, Spain (e-mail: gonzalo.seco@uab.cat).

Pontus Johannisson was with the Chalmers University of Technology, 41296 Göteborg, Sweden. He is now with the Saab AB, 41276 Göteborg, Sweden (e-mail: pontus.johannisson@saabgroup.com).

Digital Object Identifier 10.1109/TVT.2023.3246303

A great deal of research effort has been devoted to *multi-BS*[1] *localization* approaches, which exploit these novel features [19], [20], [21], [22]. Simultaneously, there has been a paradigm shift towards *single-BS localization* solutions [23], which are attractive because they require only minimal infrastructure and remove the need for inter-BS synchronization. The enabler of single-BS localization is the ability to turn multipath from foe to friend [8]: in contrast to previous beliefs that non-line-of-sight (NLoS) components have unfavorable effects on positioning, they contribute to the identifiability and accuracy of localization in mmWave multiple-input multiple-output (MIMO) systems, provided there is sufficient temporal and spatial resolution. This concept has been exploited in recent advances in localization. In particular, [24] derived both performance bounds and a method for 2D position and 1D orientation estimation, with synchronized UE and BS, based on a compressed sensing algorithm. The estimation method was refined via an atomic norm minimization approach in [25], where the performance is not limited by quantization error and grid resolution. For the same scenario of 2D position and 1D orientation, [26] showed that each NLoS path gives rise to a rank-1 Fisher information matrix (FIM) so that the UE can be localized with the LoS and a single NLoS path, or with 3 NLoS paths when the LoS is obstructed. The case of obstructed LoS was also treated in [27], without the requirement for synchronization, but still with 2D position and accordingly a single orientation angle. This concept was further extended to 3D position and 2D orientation estimation under perfect synchronization in [16], where the asymptotic case with orthogonal multipath components was studied. A further generalization was considered in [28], focusing on a direct localization approach for the massive array regime, considering a 3D position and 2D orientation estimation and a synchronized user. The more practical case considering the synchronization error as well as the Doppler shift-when the transmitter or receiver is moving-was addressed in [29], where the authors performed the FIM analysis for 2D position and 1D orientation estimation of a mobile user. In [30], the LoS 3D positioning problem using the 5G uplink channel sounding reference signals is considered, but the UE is synchronized and single-antenna, for which no orientation is defined. The closest work we identified is [31], where a hybrid model/data-driven approach for the 3D position estimation of a UE is proposed. The model-based approach is based on the underlying geometry and the angle between each two arrival directions being independent of UE orientation. However, no algorithm is proposed for orientation estimation or estimating the IP locations.

The extension of already existing methods to 3D position and 3D orientation case, however, is not trivial, since the positions (both UE and IPs) are not constrained to lie in a plane. The orientation also introduces more degrees of freedom in the geometrical equations of channel parameters, and hence, increases the complexity of search-based estimation algorithms.

[1]Recent developments relying on reconfigurable intelligent surfaces (RISs) are considered as multi-BS solutions, since a RIS acts as an additional multi-antenna BS in localization [17], [18]. For similar reasons, approaches with a single moving BS are also equivalent to multi-BS localization [9].

TABLE I
OVERVIEW OF THE RELATED WORK

Ref.	Pos.	Ori.	Clock	Bound	Method	without LoS
[24]	2D	1D	✗	✓	✓	✓
[25]	2D	1D	✗	✓	✓	✗
[26]	2D	1D	✗	✓	✗	✓
[27]	2D	1D	✓	✗	✓	✓
[16]	3D	2D	✗	✓	✗	✗
[28]	3D	2D	✗	✓	✗	✗
[29]	2D	1D	✓	✓	✓	✗
[30]	3D	✗	✗	✗	✓	✗
[31]	3D	3D	✓	✗	only pos.	✗
this work	3D	3D	✓	✓	✓	✗

In addition, the analysis of fundamental lower bounds for such a general case has not yet been conducted. The 6D localization problem was introduced in the mmWave context in [32], but has not yet been further developed. However, it has been studied in other settings, e.g., pose estimation in robotics [6] and visible light positioning [33]. In [33], a simultaneous 3D position and 3D orientation estimation using the received signal strength (RSS) for a visible light system containing multiple light emitting diodes and photodiodes is considered, and an approximate solution using direct linear transformation method is proposed. This solution is further refined using iterative algorithms for ML estimation. On a parallel track, the problem is addressed under the label of rigid body localization in [34], [35], [36], where the approach is to mount sensors with a known topology on the body. The positions of the sensors in the global coordinate frame are related to the position of the rigid body and its orientation. The sensors then form a wireless sensor network, and the position, as well as the orientation of the body, is estimated using time and/or angle measurements from sensors.

In this paper, we consider a single-BS localization scenario, where the downlink mmWave signal from a multi-antenna mmWave base station is used to estimate the 3D-position and 3D-orientation of a UE in LoS to the BS. We evaluate the lower bound on estimation error variance of position and orientation of the UE, positions of the incidence points, and the clock offset, by deriving the constrained Cramér-Rao bound (CRB) of all unknowns. This reveals that the problem is generally identifiable under a single NLoS path. To solve the corresponding high-dimensional ML problem, we propose an efficient solution, combining a geometric ad-hoc estimator to initialize a gradient descent over a product of manifolds. This solution is shown to attain the corresponding CRBs. The proposed approach is related to the literature in Table I. The main contributions of this work are the following:

- *6D localization algorithm:* We pose a high-dimensional ML estimation problem over a product of Euclidean and non-Euclidean manifolds, given the conditional probability distributions of angle-of-arrival (AoA), angle-of-departure (AoD), and time-of-arrival (ToA) measurements. The parameters of such distributions are obtained, and the root mean square error (RMSE) of the ML estimation is shown to attain the lower bounds. The ML problem is solved by gradient descent, iterating between the various manifolds, starting from a good initial solution.

- *A low-complexity estimator* We propose and evaluate a low-complexity ad-hoc estimation algorithm to initialize the solution of the ML problem, which reduces the high-dimensional problem of estimating all unknowns, to a 1-dimensional search over a finite interval combined with closed-form expressions. This recovers not only the 6D UE state, but also the UE clock bias and IP locations.
- *Fisher information and numerical analysis:* We obtain the lower bound on the estimation of the 6D user state and its clock bias, as well as the map of the environment, i.e., the positions of incidence points, and then we evaluate the impact of bandwidth, number of antennas, and number of incidence points. The analysis of the bounds indicates that in most cases a single incidence point with a priori unknown location is sufficient to render the problem identifiable, though certain configurations require several incidence points. We also evaluate a low-complexity ad-hoc and the ML 6D localization algorithms and demonstrate that it can attain the corresponding performance bounds.

The rest of the paper is organized as follows. Section II describes the system model and provides the definitions. In section III, we state the ML estimation problem, followed by a low-complexity estimation algorithm for obtaining initial solutions for iterative routines in Section IV. Subsequently, in Section V, the Fisher information analysis is done, and error bounds are derived. Section VI presents numerical results, and finally, conclusion remarks are given in Section VII.

Notations: We denote scalars, vectors, and matrices by italic, bold lowercase, and bold uppercase letters, e.g., x, $\mathbf{x}$ and $\mathbf{X}$, respectively. The element of matrix $\mathbf{X}$ in the i-th row and j-th column is indicated by $[\mathbf{X}]_{i,j}$. We also use $[\mathbf{X}]_{i:k,j:l}$ to refer to the sub-matrix lying between rows i to k and columns j to l of $\mathbf{X}$. The identity matrix of size N is shown by $\mathbf{I_N}$, whereas $\mathbf{1_N}$ and $\mathbf{0}_N$ indicate all-ones and all-zeros vectors of size N. While $\mathrm{diag}(\mathbf{x})$ is a diagonal matrix whose non-zero elements are given by $\mathbf{x}$, $\mathrm{diag}(\mathbf{X})$ is a vector composed of the diagonal elements of $\mathbf{X}$. Similarly, $\mathrm{blkdiag}(\mathbf{X}, \mathbf{Y})$ is a block-diagonal matrix made of $\mathbf{X}, \mathbf{Y}$. In order to show the expectation, trace, and vectorization operators, we use $\mathbb{E}[\cdot]$, $\mathrm{tr}[\cdot]$, and $\mathrm{vec}[\cdot]$, respectively. The transpose, and hermitian operators are symbolized using $[\cdot]^{\mathsf{T}}$ and $[\cdot]^{\mathsf{H}}$; and we consider $\odot$ and $\oslash$ in conjunction with pointwise product and division, all in the given order. The Euclidean and Frobenius norms are denoted by $\|\cdot\|$ and $\|\cdot\|_{\mathrm{F}}$, respectively.

II. System Model

We consider a downlink mmWave MIMO scenario consisting of a BS equipped with an arbitrary array of N_{BS} antennas, and a UE equipped with an arbitrary array of N_{UE} antennas, as shown in Fig. 1. Without loss of generality, both BS and UE are considered to have a single radio frequency (RF) chain.

A. Geometric Model

The BS antenna array is centered at the known position $\mathbf{p}_{\mathrm{BS}} = [p_{\mathrm{BS},x}, p_{\mathrm{BS},y}, p_{\mathrm{BS},z}]^{\mathsf{T}} \in \mathbb{R}^3$ with a known orientation, while UE antenna array is centered at the *unknown* position $\mathbf{p}_{\mathrm{UE}} = [p_{\mathrm{UE},x}, p_{\mathrm{UE},y}, p_{\mathrm{UE},z}]^{\mathsf{T}} \in \mathbb{R}^3$ with an *unknown* orientation. The

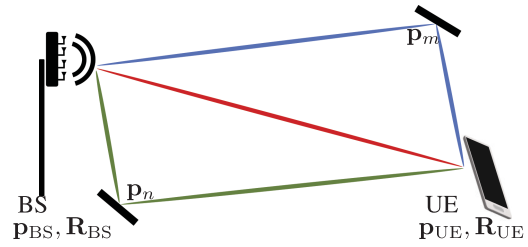

Fig. 1. Schematic of system model with a UE at unknown 3D position and unknown 3D orientation, where signals are received from LoS and NLoS paths. The UE and BS are not synchronized.

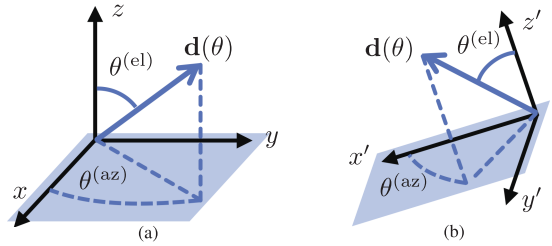

Fig. 2. (a) The global coordinate system $(x-y-z)$ and the reference orientation $\mathbf{R} = \mathbf{I}$, together with the definition of angles and their corresponding direction at orientation $\mathbf{R} = \mathbf{I}$. (b) The local coordinate system $(x'-y'-z')$ at a given orientation, together with the definition of angles and their corresponding direction at that orientation. Note that $\theta^{(\mathrm{az})} \in [0, 2\pi]$ and $\theta^{(\mathrm{el})} \in [0, \pi]$.

paths between BS and UE include the LoS, as well as $M \geq 1$ *resolvable single-bounce* NLoS paths, each corresponding to a scatterer or a reflecting point, represented by an IP at *unknown* position $\mathbf{p}_m = [p_{m,x}, p_{m,y}, p_{m,z}]^{\mathsf{T}} \in \mathbb{R}^3$, $m = 1, \ldots, M$. All positions are given in a global coordinate frame as the reference, whose axes are labeled as x, y, and z (see Fig. 2(a)).

Remark 1 (On the NLoS model): While we assume single-bounce NLoS paths, in practice multi-bounce paths may also exist. Those paths can be identified and excluded from the localization scheme, e.g., using methods such as [37] (where an iterative method based on the generalized likelihood ratio test (GLRT) and change-point detection is proposed to distinguish single-bounce and multi-bounce paths) or [38] (which progressively identifies the LoS path, single bounce, double bounce, and higher bounce paths). We also assume that all paths (including the LoS and NLoS paths) are resolvable. This is generally correct in the mmWave scenarios, due to the large bandwidth and antenna apertures.

The orientation of BS and UE describe how their antenna arrays with respect to the reference orientation are arranged. We consider rotation matrices for describing the orientations,[2] so that BS and UE orientations determine local coordinate frames, respectively described by 3×3 rotation matrices $\mathbf{R}_{\mathrm{BS}}$ and $\mathbf{R}_{\mathrm{UE}}$, in the special orthogonal group $\mathrm{SO}(3)$. In particular, we define a reference orientation where the axes are in the same direction as those of the global coordinate frame, as shown in Fig. 2(a). The local coordinate frames are thus obtained by rotating the arrays

[2]Orientations in 3D can be represented by *quaternions*, *Euler angles*, and *rotation matrices* [39]. We adopt rotation matrices.

in reference orientation through $\mathbf{R}_{\text{BS}}$ and $\mathbf{R}_{\text{UE}}$ (see Fig. 2(b)). Therefore, the given vector $\mathbf{y}$ in the global coordinate system is corresponding to $\mathbf{y}_{\text{BS}} = \mathbf{R}_{\text{BS}}^{\mathsf{T}}\mathbf{y}$ and $\mathbf{y}_{\text{UE}} = \mathbf{R}_{\text{UE}}^{\mathsf{T}}\mathbf{y}$ in BS and UE coordinate frames, respectively. We note that $\mathbf{R}_{\text{BS}}$ is known, while $\mathbf{R}_{\text{UE}}$ is unknown. The 6D localization problem refers to estimation of $\mathbf{p}_{\text{UE}}$ and $\mathbf{R}_{\text{UE}}$.

B. Signal and Channel Model

We consider downlink pilot transmission of K orthogonal frequency-division multiplexing (OFDM) symbols using N_f subcarriers over a MIMO channel, for the purpose of snapshot position and orientation estimation.[3] Considering $M+1$ (resolvable) paths indexed by $m = 0, 1, \ldots, M$ ($m = 0$ is the LoS path between the BS and the UE, which is assumed to be present, and $m \neq 0$ correspond to NLoS paths), the k-th received OFDM symbol, $k = 1, \ldots, K$, over subcarrier $n = 1, \ldots, N_f$, is given by [40]

$$y_{k,n} = \boldsymbol{w}_k^{\text{H}} \sum_{m=0}^{M} \mathbf{H}_m \boldsymbol{f}_k x_{k,n} \text{e}^{-j2\pi(n-1)\Delta_f \tau_m} + \boldsymbol{w}_k^{\text{H}} \boldsymbol{n}_{k,n}, \quad (1)$$

in which $x_{k,n}$ is a unit-modulus pilot symbol with energy $E_{\text{s}} = P_{\text{TX}}/B$, where P_{TX} is the transmit power and $B = N_f\Delta_f$ is the total bandwidth for the subcarrier spacing Δ_f; $\boldsymbol{f}_k$ is the precoding vector at BS, $\boldsymbol{w}_k$ is the combining vector at UE, with $\|\boldsymbol{f}_k\| = \|\boldsymbol{w}_k\| = 1$, $\forall k$; and $\boldsymbol{n}_{k,n} \in \mathbb{C}^{N_{\text{UE}}}$ is the complex zero-mean additive white Gaussian noise (AWGN) with covariance matrix $n_0 N_0 \mathbf{I}_{N_{\text{UE}}}$, where N_0 is the noise power spectral density (PSD), and n_0 is the UE noise figure. Furthermore, each path m is characterized by a ToA τ_m and a channel matrix $\mathbf{H}_m \triangleq h_m\, \mathbf{a}_{\text{UE}}(\boldsymbol{\theta}_{\text{A},m})\mathbf{a}_{\text{BS}}^{\mathsf{T}}(\boldsymbol{\theta}_{\text{D},m})$, where $h_m = h_{\text{R},m} + jh_{\text{I},m}$ is the complex channel gain; $\mathbf{a}_{\text{UE}}(\boldsymbol{\theta}_{\text{A},m})$ and $\mathbf{a}_{\text{BS}}(\boldsymbol{\theta}_{\text{D},m})$ are the array response vectors, where $\boldsymbol{\theta}_{\text{A},m} = [\theta_{\text{A},m}^{(\text{az})}, \theta_{\text{A},m}^{(\text{el})}]^{\mathsf{T}}$ and $\boldsymbol{\theta}_{\text{D},m} = [\theta_{\text{D},m}^{(\text{az})}, \theta_{\text{D},m}^{(\text{el})}]^{\mathsf{T}}$ show the AoA and AoD in azimuth and elevation (as defined in Fig. 2(b) and Section II-C), respectively. The array response vectors are given by

$$[\mathbf{a}_{\text{UE}}(\boldsymbol{\theta}_{\text{A},m})]_n = \exp\left(j\frac{2\pi}{\lambda}[\boldsymbol{\Delta}_{\text{UE}}]_{1:3,n}^{\mathsf{T}}\mathbf{d}(\boldsymbol{\theta}_{\text{A},m})\right), \quad (2a)$$

$$[\mathbf{a}_{\text{BS}}(\boldsymbol{\theta}_{\text{D},m})]_n = \exp\left(j\frac{2\pi}{\lambda}[\boldsymbol{\Delta}_{\text{BS}}]_{1:3,n}^{\mathsf{T}}\mathbf{d}(\boldsymbol{\theta}_{\text{D},m})\right), \quad (2b)$$

in which λ is the wavelength at the carrier frequency f_c; and $\boldsymbol{\Delta}_{\text{UE}} \triangleq [\mathbf{x}_{\text{UE},1}, \ldots, \mathbf{x}_{\text{UE},N_{\text{UE}}}] \in \mathbb{R}^{3\times N_{\text{UE}}}$ and $\boldsymbol{\Delta}_{\text{BS}} \triangleq [\mathbf{x}_{\text{BS},1}, \ldots, \mathbf{x}_{\text{BS},N_{\text{BS}}}] \in \mathbb{R}^{3\times N_{\text{BS}}}$ contain coordinates of antenna elements in reference orientation, with respect to the UE and the BS coordinate frames (i.e., 3D displacements from the phase center), respectively. In (2), we have introduced

$$\mathbf{d}(\boldsymbol{\phi}) = [\sin\phi^{(\text{el})}\cos\phi^{(\text{az})}, \sin\phi^{(\text{el})}\sin\phi^{(\text{az})}, \cos\phi^{(\text{el})}]^{\mathsf{T}}, \quad (3)$$

which describes the unit-norm direction of arrival (for $\boldsymbol{\phi} = \boldsymbol{\theta}_{\text{A},m}$) and unit-norm direction of departure (for $\boldsymbol{\phi} = \boldsymbol{\theta}_{\text{D},m}$) for path m, in UE and BS coordinate frames, respectively.

[3]We assume a slow fading channel, which does not vary over the duration of the pilot transmission.

C. Relation Between Geometric Model and Channel Model

Corresponding to the AoAs, the unit-norm arrival directions $\mathbf{d}_{\text{A},m} = \mathbf{d}(\boldsymbol{\theta}_{\text{A},m})$ are given, in the UE coordinate frame, by

$$\mathbf{d}_{\text{A},m} = \begin{cases} \mathbf{R}_{\text{UE}}^{\mathsf{T}}(\mathbf{p}_{\text{BS}} - \mathbf{p}_{\text{UE}})/\|\mathbf{p}_{\text{BS}} - \mathbf{p}_{\text{UE}}\| & m = 0 \\ \mathbf{R}_{\text{UE}}^{\mathsf{T}}(\mathbf{p}_m - \mathbf{p}_{\text{UE}})/\|\mathbf{p}_m - \mathbf{p}_{\text{UE}}\| & m \neq 0, \end{cases} \quad (4)$$

which define the AoAs as $\theta_{\text{A},m}^{(\text{az})} = \text{atan2}([\mathbf{d}_{\text{A},m}]_2, [\mathbf{d}_{\text{A},m}]_1)$ and $\theta_{\text{A},m}^{(\text{el})} = \text{acos}([\mathbf{d}_{\text{A},m}]_3)$, where acos is the inverse cosine and atan2 is the four-quadrant inverse tangent. Similarly, using the unit-norm departure directions $\mathbf{d}_{\text{D},m} = \mathbf{d}(\boldsymbol{\theta}_{\text{D},m})$ given by

$$\mathbf{d}_{\text{D},m} = \begin{cases} \mathbf{R}_{\text{BS}}^{\mathsf{T}}(\mathbf{p}_{\text{UE}} - \mathbf{p}_{\text{BS}})/\|\mathbf{p}_{\text{UE}} - \mathbf{p}_{\text{BS}}\| & m = 0 \\ \mathbf{R}_{\text{BS}}^{\mathsf{T}}(\mathbf{p}_m - \mathbf{p}_{\text{BS}})/\|\mathbf{p}_m - \mathbf{p}_{\text{BS}}\| & m \neq 0, \end{cases} \quad (5)$$

in BS coordinate frame, the AoDs are determined as $\theta_{\text{D},m}^{(\text{az})} = \text{atan2}([\mathbf{d}_{\text{D},m}]_2, [\mathbf{d}_{\text{D},m}]_1)$ and $\theta_{\text{D},m}^{(\text{el})} = \text{acos}([\mathbf{d}_{\text{D},m}]_3)$. Fig. 2(b) shows how AoDs and AoAs and their corresponding directions are defined. Note that the arrows corresponding to the arrival directions point towards the BS/IPs, and not the UE.

Finally, denoting the propagation speed by c and the *unknown* clock bias between the UE and the BS by b, one can express ToAs as

$$\tau_m = \begin{cases} \|\mathbf{p}_{\text{UE}} - \mathbf{p}_{\text{BS}}\|/c + b & m = 0 \\ (\|\mathbf{p}_m - \mathbf{p}_{\text{BS}}\| + \|\mathbf{p}_{\text{UE}} - \mathbf{p}_m\|)/c + b & m \neq 0. \end{cases} \quad (6)$$

The aggregated vectors $\boldsymbol{\theta}_{\text{A}} = [\boldsymbol{\theta}_{\text{A},0}^{\mathsf{T}}, \boldsymbol{\theta}_{\text{A},1}^{\mathsf{T}}, \ldots, \boldsymbol{\theta}_{\text{A},M}^{\mathsf{T}}]^{\mathsf{T}}$, $\boldsymbol{\theta}_{\text{D}} = [\boldsymbol{\theta}_{\text{D},0}^{\mathsf{T}}, \boldsymbol{\theta}_{\text{D},1}^{\mathsf{T}}, \ldots, \boldsymbol{\theta}_{\text{D},M}^{\mathsf{T}}]^{\mathsf{T}}$, $\boldsymbol{\tau} = [\tau_0, \ldots, \tau_M]^{\mathsf{T}}$, and $\boldsymbol{\eta} = [\boldsymbol{\theta}_{\text{A}}^{\mathsf{T}}, \boldsymbol{\theta}_{\text{D}}^{\mathsf{T}}, \boldsymbol{\tau}^{\mathsf{T}}]^{\mathsf{T}}$ are defined to be used later.

III. 6D Localization Methodology

A. Two-Stage Localization and Problem Decomposition

We consider a two-stage localization scheme and decompose the problem into a channel parameters estimation routine, followed by a localization routine. The channel estimation routine determines the marginal posterior densities of the channel parameters (in the form of estimates and the associated uncertainties), based on the observations (1). The localization routine uses the output of the channel parameters estimator to determine the 6D state of the UE. We consider the contribution of this paper to provide a solution to the second sub-problem, while considering a generic channel parameter estimator.

1) Channel Parameters Estimation: There exists a variety of channel parameter estimators in the literature, including ESPRIT [41], generalized approximate message passing [40], [42], orthogonal matching pursuit [24], sparse Bayesian learning [43], tensor decomposition [44], and RIMAX/SAGE [45]. We assume an arbitrary estimator is applied to obtain an estimate of $\boldsymbol{\eta}$. We denote by $\hat{\boldsymbol{\eta}} = [\hat{\boldsymbol{\theta}}_{\text{A}}^{\mathsf{T}}, \hat{\boldsymbol{\theta}}_{\text{D}}^{\mathsf{T}}, \hat{\boldsymbol{\tau}}^{\mathsf{T}}]^{\mathsf{T}}$, the vector of estimated channel parameters, also referred to as the vector of *measurements*. For each parameter, there is also an associated uncertainty, which leads to the following likelihood functions. For the ToA measurements, we assume a multivariate Gaussian distribution [46],

[47]

$$p(\hat{\boldsymbol{\tau}}|\boldsymbol{\tau}) = \frac{1}{\sqrt{(2\pi)^{M+1}|\Sigma_{\boldsymbol{\tau}}|}} e^{-\frac{1}{2}(\hat{\boldsymbol{\tau}}-\boldsymbol{\tau})^{\mathsf{T}}\Sigma_{\boldsymbol{\tau}}^{-1}(\hat{\boldsymbol{\tau}}-\boldsymbol{\tau})}, \tag{7}$$

where $\Sigma_{\boldsymbol{\tau}} = \mathrm{diag}(\sigma_0^2, \ldots, \sigma_M^2)$. Note that both $\hat{\tau}_m$ and σ_m^2 are provided by the channel parameter estimator. For the AoAs and AoDs, we follow [48] and use a Von Mises distribution, which can be interpreted as a Gaussian distribution over the 1D manifold of angles [49, Chapter 3]. Correspondingly,[4]

$$\begin{aligned} &p(\hat{\boldsymbol{\theta}}_{\mathrm{A},m}|\boldsymbol{\theta}_{\mathrm{A},m}) \\ &= \exp\left(\kappa_{\mathrm{A},m}^{(\mathrm{az})}\cos(\hat{\theta}_{\mathrm{A},m}^{(\mathrm{az})} - \theta_{\mathrm{A},m}^{(\mathrm{az})})\right) / \left(2\pi I_0(\kappa_{\mathrm{A},m}^{(\mathrm{az})})\right) \\ &\quad \times \exp\left(\kappa_{\mathrm{A},m}^{(\mathrm{el})}\cos(\hat{\theta}_{\mathrm{A},m}^{(\mathrm{el})} - \theta_{\mathrm{A},m}^{(\mathrm{el})})\right) / \left(2\pi I_0(\kappa_{\mathrm{A},m}^{(\mathrm{el})})\right), \end{aligned} \tag{8a}$$

$$\begin{aligned} &p(\hat{\boldsymbol{\theta}}_{\mathrm{D},m}|\boldsymbol{\theta}_{\mathrm{D},m}) \\ &= \exp\left(\kappa_{\mathrm{D},m}^{(\mathrm{az})}\cos(\hat{\theta}_{\mathrm{D},m}^{(\mathrm{az})} - \theta_{\mathrm{D},m}^{(\mathrm{az})})\right) / \left(2\pi I_0(\kappa_{\mathrm{D},m}^{(\mathrm{az})})\right) \\ &\quad \times \exp\left(\kappa_{\mathrm{D},m}^{(\mathrm{el})}\cos(\hat{\theta}_{\mathrm{D},m}^{(\mathrm{el})} - \theta_{\mathrm{D},m}^{(\mathrm{el})})\right) / \left(2\pi I_0(\kappa_{\mathrm{D},m}^{(\mathrm{el})})\right), \end{aligned} \tag{8b}$$

where $\kappa_{\mathrm{A},m}^{(\mathrm{az})}$, $\kappa_{\mathrm{A},m}^{(\mathrm{el})}$, $\kappa_{\mathrm{D},m}^{(\mathrm{az})}$, and $\kappa_{\mathrm{D},m}^{(\mathrm{el})}$, are the non-negative concentration parameters of m-th AoA and m-th AoD, in azimuth and elevation, respectively, and $I_0(\cdot)$ is the modified Bessel function of order 0. Again, both the estimated angles and the corresponding concentration parameters are assumed to be provided by the channel parameter estimator.

2) Location Parameters Estimation: The localization problem is formulated as the maximum likelihood estimation

$$\hat{\mathbf{R}}_{\mathrm{UE}}, \hat{\boldsymbol{\zeta}} = \arg\max_{\mathbf{R}_{\mathrm{UE}},\boldsymbol{\zeta}} \ln p(\hat{\boldsymbol{\eta}}|\boldsymbol{\eta}(\mathbf{R}_{\mathrm{UE}},\boldsymbol{\zeta})),\ \mathbf{R}_{\mathrm{UE}} \in \mathrm{SO}(3), \tag{9}$$

where $\boldsymbol{\zeta} = [\mathbf{p}_{\mathrm{UE}}^{\mathsf{T}}, \mathbf{p}_1^{\mathsf{T}}, \ldots, \mathbf{p}_M^{\mathsf{T}}, b]^{\mathsf{T}} \in \mathbb{R}^{3(M+1)+1}$ and the likelihood $p(\hat{\boldsymbol{\eta}}|\boldsymbol{\eta}(\mathbf{R}_{\mathrm{UE}},\boldsymbol{\zeta}))$ is expressed of the underlying geometry. The likelihood is of the form

$$\begin{aligned} p\left(\hat{\boldsymbol{\eta}}|\boldsymbol{\eta}(\mathbf{R}_{\mathrm{UE}},\boldsymbol{\zeta})\right) = &\ p\left(\hat{\boldsymbol{\theta}}_{\mathrm{A}}|\boldsymbol{\theta}_{\mathrm{A}}(\mathbf{R}_{\mathrm{UE}},\boldsymbol{\zeta})\right) \\ &\times p\left(\hat{\boldsymbol{\theta}}_{\mathrm{D}}|\boldsymbol{\theta}_{\mathrm{D}}(\boldsymbol{\zeta})\right) \times p\left(\hat{\boldsymbol{\tau}}|\boldsymbol{\tau}(\boldsymbol{\zeta})\right), \end{aligned} \tag{10}$$

in which, by overloading the notation for cosines, we have

$$p\left(\hat{\boldsymbol{\theta}}_{\mathrm{A}}|\boldsymbol{\theta}_{\mathrm{A}}(\mathbf{R}_{\mathrm{UE}},\boldsymbol{\zeta})\right) \propto \exp\left(\boldsymbol{\kappa}_{\mathrm{A}}^{\mathsf{T}}\cos\left(\hat{\boldsymbol{\theta}}_{\mathrm{A}} - \boldsymbol{\theta}_{\mathrm{A}}(\mathbf{R}_{\mathrm{UE}},\boldsymbol{\zeta})\right)\right), \tag{11a}$$

$$p\left(\hat{\boldsymbol{\theta}}_{\mathrm{D}}|\boldsymbol{\theta}_{\mathrm{D}}(\boldsymbol{\zeta})\right) \propto \exp\left(\boldsymbol{\kappa}_{\mathrm{D}}^{\mathsf{T}}\cos\left(\hat{\boldsymbol{\theta}}_{\mathrm{D}} - \boldsymbol{\theta}_{\mathrm{D}}(\boldsymbol{\zeta})\right)\right), \tag{11b}$$

where $\boldsymbol{\kappa}_{\mathrm{A}}$ and $\boldsymbol{\kappa}_{\mathrm{D}}$ are $2(M+1)\times 1$ vectors aggregating the concentration parameters of Von Mises distributions corresponding to the angle estimates in $\hat{\boldsymbol{\theta}}_{\mathrm{A}}$ and $\hat{\boldsymbol{\theta}}_{\mathrm{D}}$, respectively. Considering the negative log-likelihood $\mathcal{L}(\mathbf{R}_{\mathrm{UE}},\boldsymbol{\zeta}) = -\ln p(\hat{\boldsymbol{\eta}}|\boldsymbol{\eta}(\mathbf{R}_{\mathrm{UE}},\boldsymbol{\zeta}))$, the ML estimation (9) can be equivalently written as the constrained minimization

$$\min_{\mathbf{R}_{\mathrm{UE}},\boldsymbol{\zeta}} \mathcal{L}(\mathbf{R}_{\mathrm{UE}},\boldsymbol{\zeta}), \tag{12a}$$

$$\text{s.t. } \mathbf{R}_{\mathrm{UE}}^{\mathsf{T}}\mathbf{R}_{\mathrm{UE}} = \mathbf{I},\ \det(\mathbf{R}_{\mathrm{UE}}) = +1. \tag{12b}$$

where

$$\begin{aligned} \mathcal{L}(\mathbf{R}_{\mathrm{UE}},\boldsymbol{\zeta}) = &\frac{1}{2}(\hat{\boldsymbol{\tau}} - \boldsymbol{\tau}(\boldsymbol{\zeta}))^{\mathsf{T}}\Sigma_{\boldsymbol{\tau}}^{-1}(\hat{\boldsymbol{\tau}} - \boldsymbol{\tau}(\boldsymbol{\zeta})) \\ &- \boldsymbol{\kappa}_{\mathrm{A}}^{\mathsf{T}}\cos(\hat{\boldsymbol{\theta}}_{\mathrm{A}} - \boldsymbol{\theta}_{\mathrm{A}}(\mathbf{R}_{\mathrm{UE}},\boldsymbol{\zeta})) \\ &- \boldsymbol{\kappa}_{\mathrm{D}}^{\mathsf{T}}\cos(\hat{\boldsymbol{\theta}}_{\mathrm{D}} - \boldsymbol{\theta}_{\mathrm{D}}(\boldsymbol{\zeta})). \end{aligned} \tag{13}$$

However, solving the optimization problem (12) using the classical optimization tools is difficult [33], due to the unitary constraint (12b) on the rotation matrix $\mathbf{R}_{\mathrm{UE}}$. In addition, the objective function $\mathcal{L}(\mathbf{R}_{\mathrm{UE}},\boldsymbol{\zeta})$ is highly nonlinear and non-convex, and iterative algorithms for solving (12) might reach local optima, if initialized by the points far from the global solution. To address these challenges, we propose a two-step approach: first, we determine an initial ad-hoc estimate of unknowns from geometric arguments, being then refined by a gradient descent of the objective function. The iterative algorithm is explained in the following, while the process to determine an initial point is deferred until Section IV.

B. An Iterative Algorithm for ML Estimation

As (12) involves optimization over non-Euclidean manifolds, a suitable optimization tool must be applied. We first present a method for such optimization before applying that to our 6D localization problem.

1) Overview of a Method for Optimization Over Non-Euclidean Manifolds: Consider the optimization problem

$$\hat{\mathsf{X}} = \arg\min_{\mathsf{X}\in\mathcal{M}} f(\mathsf{X}), \tag{14}$$

where $f:\mathcal{M}\to\mathbb{R}$ is a smooth function over the (possibly) non-Euclidean manifold $\mathcal{M}$, and X denotes the (possibly) non-Euclidean parameter. We exploit the Riemannian gradient descent algorithm, which is a first-order technique analogous to the standard gradient descent algorithm, where the Riemannian gradient is obtained by projection of the classical gradients to the tangent spaces. Starting from the initial point $\hat{\mathsf{X}}^{(0)}$, the algorithm iterates

$$\hat{\mathsf{X}}^{(k+1)} = \mathcal{R}_{\hat{\mathsf{X}}^{(k)}}\left(-\varepsilon_k \mathcal{P}_{\hat{\mathsf{X}}^{(k)}}\left[\partial f(\mathsf{X})/\partial \mathsf{X}\right]_{\mathsf{X}=\hat{\mathsf{X}}^{(k)}}\right), \tag{15}$$

where $\mathcal{P}_{\mathsf{X}}(\cdot)$ is an orthogonal projection onto the tangent space at X, $\mathcal{R}_{\mathsf{X}}(\cdot)$ is a retraction from the tangent space onto $\mathcal{M}$, and $\varepsilon_k > 0$ is a suitable step size. Intuitively, the gradient is calculated, and projected to the tangent space (to follow the space of $\mathcal{M}$ as closely as possible), the value at step k is updated, and then the updated value is normalized back into the $\mathcal{M}$. Relevant for us is $\mathcal{M} = \mathrm{SO}(3)$. Example projection and retraction operations for the Riemannian gradient descent algorithm are given by [50, Eqs. (7.32) and (7.22)]:

$$\mathcal{P}_{\mathbf{X}}(\mathbf{U}) = \mathbf{X}(\mathbf{X}^{\mathsf{T}}\mathbf{U} - \mathbf{U}^{\mathsf{T}}\mathbf{X})/2, \tag{16a}$$

[4]While it is shown in [16] that azimuth and elevation angles are correlated in general, we neglect the correlation and assume factorized likelihoods, for the sake of tractability. We will later evaluate the impact of this independence assumption (see Section VI-B).

$$\mathcal{R}_{\mathbf{X}}(\mathbf{U}) = (\mathbf{X}+\mathbf{U})(\mathbf{I}_3 + \mathbf{U}^{\mathsf{T}}\mathbf{U})^{-1/2}. \tag{16b}$$

On the other hand, for $\mathcal{M} = \mathbb{R}^n$, $\mathcal{P}_{\mathbf{X}}(\mathbf{U}) = \mathbf{U}$, $\mathcal{R}_{\mathbf{X}}(\mathbf{U}) = \mathbf{x} + \mathbf{U}$, leading to classical gradient descent.

2) Solving the ML Estimation Problem: Inspired by the coordinate descent algorithm [51, Sec. 9.3], we decompose the unknowns, and apply different optimization algorithms for the estimation of $\mathbf{R}_{\text{UE}}$ and the rest of unknowns $\boldsymbol{\zeta}$, which belong to the Euclidean space. We then consider the Riemannian gradient descent algorithm to optimize $\mathbf{R}_{\text{UE}}$ on the SO(3) manifold, as

$$\hat{\mathbf{R}}_{\text{UE}}^{(k+1)} = \mathcal{R}_{\hat{\mathbf{R}}_{\text{UE}}^{(k)}}\left(-\varepsilon_k \mathcal{P}_{\hat{\mathbf{R}}_{\text{UE}}^{(k)}}\left(\partial\mathcal{L}/\partial\mathbf{R}_{\text{UE}}\right)|_{\hat{\mathbf{R}}_{\text{UE}}^{(k)},\hat{\boldsymbol{\zeta}}^{(k)}}\right), \tag{17}$$

with the projection and retraction operators as defined in (16), and ε_k being the step size obtained using a backtracking line-search [50]. We also use the trust region algorithm [51, Sec. 11.2] to optimize $\boldsymbol{\zeta}$ in the Euclidean space, considering the updated rotation matrix. Then we iterate this algorithm until a stopping criterion is met. The partial derivatives $\partial\mathcal{L}/\partial\mathbf{R}_{\text{UE}}$ and $\partial\mathcal{L}/\partial\boldsymbol{\zeta}$ are obtained using the chain rule by including the partial derivatives of channel parameters w.r.t. localization parameters given in Appendix A. The above method requires initial estimates $\hat{\mathbf{R}}_{\text{UE}}^{(0)}$ and $\hat{\boldsymbol{\zeta}}^{(0)}$, which will be provided by the ad-hoc initial estimator.

IV. Ad-Hoc Initial Estimate

As stated earlier, the ML problem is a nonlinear non-convex optimization, and the elaborated iterative algorithm might reach local optima if the initial values are not given properly. In the following, we propose a simple (with linear complexity in the number of IPs and involving only a 1D line search) sequential scheme for obtaining initial estimates of localization unknowns based on the estimates of AoAs, AoDs, and ToAs: First, we estimate $\mathbf{R}_{\text{UE}}$ only from the estimated AoAs and AoDs, without any knowledge of $\mathbf{p}_{\text{UE}}$, $\mathbf{p}_1, \ldots, \mathbf{p}_M$, and b. Second, given the estimated $\mathbf{R}_{\text{UE}}$, we estimate $\mathbf{p}_{\text{UE}}$, $\mathbf{p}_1, \ldots, \mathbf{p}_M$ from TDoA measurements. Finally, we estimate the clock bias b using the estimated positions and ToAs. The algorithm, therefore, takes the measurements $\hat{\boldsymbol{\theta}}_{\text{A}}$, $\hat{\boldsymbol{\theta}}_{\text{D}}$, and $\hat{\boldsymbol{\tau}}$ as input, but we omit the "hat" ($\hat{\cdot}$) of the measurements, only in this section, for the notational convenience. Note that the values are not confused with the true *unknown* channel parameters.

A. Step 1: Estimation of UE Rotation Matrix

Our approach to estimate the UE rotation matrix from the AoAs $\boldsymbol{\theta}_{\text{A},m}$ and AoDs $\boldsymbol{\theta}_{\text{D},m}$ (and corresponding unit vectors $\mathbf{d}(\boldsymbol{\theta}_{\text{A},m})$ and $\mathbf{d}(\boldsymbol{\theta}_{\text{D},m})$) is based on an axis-angle representation of its orientation. Consider the LoS arrival and departure directions $\mathbf{d}_{\text{A},0}$ and $\mathbf{d}_{\text{D},0}$, which are along LoS path, while in opposite directions in the global coordinate frame. Hence,

$$\mathbf{R}_{\text{BS}}\mathbf{d}_{\text{D},0} = -\mathbf{R}_{\text{UE}}\mathbf{d}_{\text{A},0}. \tag{18}$$

This equation has infinitely many solutions for $\mathbf{R}_{\text{UE}}$, satisfying both (18) and the orthogonality constraint, among which, one is the true $\mathbf{R}_{\text{UE}}$.

1) Characterizing the Solutions to (18): We first find a solution for $\mathbf{R}_{\text{UE}}$ in (18), denoted by $\widetilde{\mathbf{R}} \in \text{SO}(3)$. Multiplying $\widetilde{\mathbf{R}}$ with a rotation $\psi \in [0, 2\pi)$ around $\mathbf{d}_{\text{A},0}$ yields all rotation matrices that satisfy (18).

Lemma 1: One solution for (18) is given by

$$\widetilde{\mathbf{R}} = \mathbf{I} + [\mathbf{d}]_\times + \frac{1}{1 - \mathbf{d}_{\text{A},0}^{\mathsf{T}}\mathbf{R}_{\text{BS}}\mathbf{d}_{\text{D},0}}[\mathbf{d}]_\times^2, \tag{19}$$

where $\mathbf{d} = [d_1, d_2, d_3]^{\mathsf{T}} \triangleq -\mathbf{d}_{\text{A},0} \times \mathbf{R}_{\text{BS}}\mathbf{d}_{\text{D},0}$, and

$$[\mathbf{d}]_\times \triangleq \begin{bmatrix} 0 & -d_3 & d_2 \\ d_3 & 0 & -d_1 \\ -d_2 & d_1 & 0 \end{bmatrix}. \tag{20}$$

Proof: Let us define $\tilde{\mathbf{d}} = -\mathbf{R}_{\text{BS}}\mathbf{d}_{\text{D},0}$. The result follows from Rodrigues' formula, by rotating $\mathbf{d}_{\text{A},0}$ to $\tilde{\mathbf{d}}$ with rotation axis $\mathbf{d}_{\text{A},0} \times \tilde{\mathbf{d}}$ [52, Section 9.6.2]. □

Lemma 2: The transformation matrix describing rotations by the angle $\psi \in [0, 2\pi)$ around the arbitrary unit-norm vector $\mathbf{u}$ is given by $\mathbf{Q}_{\mathbf{u}}(\psi) = [\mathbf{u}]_\times \sin\psi + (\mathbf{I} - \mathbf{u}\mathbf{u}^{\mathsf{T}})\cos\psi + \mathbf{u}\mathbf{u}^{\mathsf{T}}$.

Proof: The result follows from Rodrigues' formula [52, Section 9.6.2]. □

The rotation matrices $\mathbf{R}_{\text{UE}}$ satisfying (18) are thus characterized as

$$\mathbf{R}(\psi) = \widetilde{\mathbf{R}}\mathbf{Q}_{\mathbf{d}_{\text{A},0}}(\psi),\ \forall\psi \in [0, 2\pi). \tag{21}$$

It is easily verified that (18) holds for $\forall\psi \in [0, 2\pi)$, since $-\widetilde{\mathbf{R}}\mathbf{Q}_{\mathbf{d}_{\text{A},0}}(\psi)\mathbf{d}_{\text{A},0} = -\widetilde{\mathbf{R}}\mathbf{d}_{\text{A},0} = \mathbf{R}_{\text{BS}}\mathbf{d}_{\text{D},0}$, where the first transition is due to a rotation around an axis leaving that axis invariant, and the second transition due to Lemma 1. What remains is now to determine ψ based on the NLoS paths.

2) Rotation Estimation Based on NLoS AoAs and AoDs: We now determine the angle $\psi \in [0, 2\pi)$, so that the combined rotation resulting from $\widetilde{\mathbf{R}}$ and $\mathbf{Q}_{\mathbf{d}_{\text{A},0}}(\psi)$, i.e., $\mathbf{R}(\psi) = \widetilde{\mathbf{R}}\mathbf{Q}_{\mathbf{d}_{\text{A},0}}(\psi)$, leads to the arrival directions $\mathbf{d}_{\text{A},m}$, $m = 1, \ldots, M$. To determine ψ, we note the following (see Fig. 1):

- The departure directions $\mathbf{d}_{\text{D},m}$, $m = 1, \ldots, M$, determine the half-lines $\ell_{\text{D},m}(\mathbf{p}_{\text{BS}}, \mathbf{R}_{\text{BS}}, \mathbf{d}_{\text{D},m}) = \{\mathbf{p} \in \mathbb{R}^3 : \mathbf{p} = \mathbf{p}_{\text{BS}} + t_{\text{D},m}\mathbf{R}_{\text{BS}}\mathbf{d}_{\text{D},m},\ t_{\text{D},m} \geq 0\}$, in the global coordinate frame.
- Under UE rotation represented by $\mathbf{R}(\psi)$, the arrival directions $\mathbf{d}_{\text{A},m}$, $m = 1, \ldots, M$, determine the half-lines $\ell_{\text{A},m}(\mathbf{p}_{\text{UE}}, \mathbf{R}(\psi), \mathbf{d}_{\text{A},m}) = \{\mathbf{p} \in \mathbb{R}^3 : \mathbf{p} = \mathbf{p}_{\text{UE}} + t_{\text{A},m}\ \mathbf{R}(\psi)\mathbf{d}_{\text{A},m},\ t_{\text{A},m} \geq 0\}$, for any given $\psi \in [0, 2\pi)$, in the global coordinate frame. See Fig. 3.
- With the correct ψ, the half-lines $\ell_{\text{D},m}(\mathbf{p}_{\text{BS}}, \mathbf{R}_{\text{BS}}, \mathbf{d}_{\text{D},m})$ and $\ell_{\text{A},m}(\mathbf{p}_{\text{UE}}, \mathbf{R}(\psi), \mathbf{d}_{\text{A},m})$ intersect at the incidence point $\mathbf{p}_m$ (in the absence of noise).

However, (i) neither $\mathbf{p}_{\text{UE}}$ nor $\mathbf{p}_m$ are known; (ii) the half-lines might not necessarily intersect due to the noisy measurements.[5] To tackle the first challenge, we note that the argument that the half-lines intersect under the correct value of ψ is true for any scaling of the global coordinate system. We express $\mathbf{p}_{\text{UE}} =$

[5]They form a pair of so-called *skew lines*, i.e., lines in 3D that do not intersect, while not being parallel.

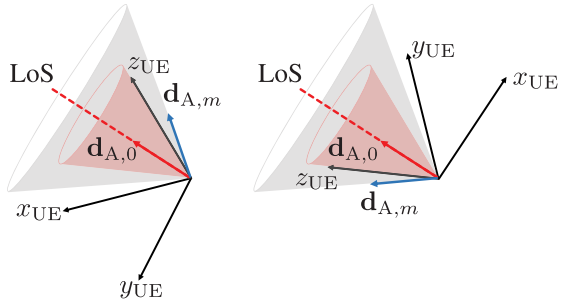

Fig. 3. The example NLoS arrival direction $\mathbf{d}_{\mathrm{A},m}$ rotates, in the global coordinate frame, while maintaining the same angle $\boldsymbol{\theta}_{\mathrm{A},m}$ in UE coordinate frame, on the lateral surface of a cone (the gray cone in this figure) with axis $\mathbf{d}_{\mathrm{A},0}$, and apex angle equal to the angle between $\mathbf{d}_{\mathrm{A},0}$ and $\mathbf{d}_{\mathrm{A},m}$, when the rotation around axis $\mathbf{d}_{\mathrm{A},0}$ is applied. The figure illustrates two snapshots of such rotation.

$\mathbf{p}_{\mathrm{BS}} + \rho_0 \mathbf{R}_{\mathrm{BS}} \mathbf{d}_{\mathrm{D},0}$, where $\rho_0 = \|\mathbf{p}_{\mathrm{BS}} - \mathbf{p}_{\mathrm{UE}}\|$. Any point $\mathbf{p} \in \mathbb{R}^3$ can be expressed as $\mathbf{p} = \mathbf{p}_{\mathrm{BS}} + \rho \mathbf{R}_{\mathrm{BS}} \mathbf{d}_{\mathrm{D}}$, with suitable ρ and $\mathbf{d}_{\mathrm{D}}$, where $\mathbf{d}_{\mathrm{D}}$ is a unit-norm vector. Given any $r > 0$, we can define a scaled system (with scaling r/ρ_0) with the BS location as an invariant point:

$$\mathbf{p}(r) = \mathbf{p}_{\mathrm{BS}} + \frac{r}{\rho_0} \rho \mathbf{R}_{\mathrm{BS}} \mathbf{d}_{\mathrm{D}}, \tag{22}$$

and in particular

$$\mathbf{p}_{\mathrm{UE}}(r) = \mathbf{p}_{\mathrm{BS}} + \frac{r}{\rho_0} \rho_0 \mathbf{R}_{\mathrm{BS}} \mathbf{d}_{\mathrm{D},0}. \tag{23}$$

Without loss of generality, we set $r = 1$ so that $\mathbf{p}_{\mathrm{UE}}(r = 1)$ is known. Hence, in the scaled coordinate system with $r = 1$, $\ell_{\mathrm{A},m}(\mathbf{p}_{\mathrm{UE}}(r), \mathbf{R}(\psi), \mathbf{d}_{\mathrm{A},m})$ and $\ell_{\mathrm{D},m}(\mathbf{p}_{\mathrm{UE}}(r), \mathbf{R}(\psi), \mathbf{d}_{\mathrm{D},m})$ intersect for the correct value of ψ, $\forall m$, in the absence of noise. To cope with the second challenge (measurement noise), we use the distance between skew lines in the least squares objective. In particular, the shortest distance $\delta_m(\psi)$ between the half-lines $\ell_{\mathrm{D},m}(\mathbf{p}_{\mathrm{BS}}, \mathbf{R}_{\mathrm{BS}}, \mathbf{d}_{\mathrm{D},m})$ and $\ell_{\mathrm{A},m}(\mathbf{p}'_{\mathrm{UE}}, \mathbf{R}(\psi), \mathbf{d}_{\mathrm{A},m})$ is obtained from the solution of parametric optimization

$$\delta_m^2(\psi) = \min_{\mathbf{t}_m \geq \mathbf{0}} D_m^2(\mathbf{t}_m, \mathbf{R}(\psi)),\ m > 0, \tag{24}$$

where $\mathbf{t}_m = [t_{\mathrm{D},m}, t_{\mathrm{A},m}]^{\mathsf{T}}$ and $D_m^2(\mathbf{t}_m, \mathbf{R}(\psi)) = \|(\mathbf{p}_{\mathrm{BS}} + t_{\mathrm{D},m} \mathbf{R}_{\mathrm{BS}} \mathbf{d}_{\mathrm{D},m}) - (\mathbf{p}_{\mathrm{UE}}(1) + t_{\mathrm{A},m} \mathbf{R}(\psi) \mathbf{d}_{\mathrm{A},m})\|^2$. The optimization (24) is a quadratic convex problem, and the solution of that is provided in Appendix B. Combining the minimum distances, we estimate ψ as

$$\hat{\psi} = \arg \min_{\psi \in [0, 2\pi)} \|\boldsymbol{\delta}(\psi)\|, \tag{25}$$

where $\boldsymbol{\delta}(\psi) = [\delta_1(\psi), \ldots, \delta_M(\psi)]^{\mathsf{T}}$, and accordingly, the estimate of $\mathbf{R}_{\mathrm{UE}}$ is given by $\hat{\mathbf{R}}_{\mathrm{UE}} = \mathbf{R}(\hat{\psi})$, with $\mathbf{R}(\psi)$ characterized as in (21).

B. Step 2: Estimation of Positions

We obtain the auxiliary points $\mathbf{p}_m(r = 1)$ in the scaled coordinate system induced by (22), as the nearest points to the half-lines $\ell_{\mathrm{D},m}(\mathbf{p}_{\mathrm{BS}}, \mathbf{R}_{\mathrm{BS}}, \mathbf{d}_{\mathrm{D},m})$ and $\ell_{\mathrm{A},m}(\mathbf{p}_{\mathrm{UE}}(1), \hat{\mathbf{R}}_{\mathrm{UE}}, \mathbf{d}_{\mathrm{A},m})$ in a least-squares sense (considering the lines from UE and BS as full lines, rather than half-lines, for computational complexity considerations), using

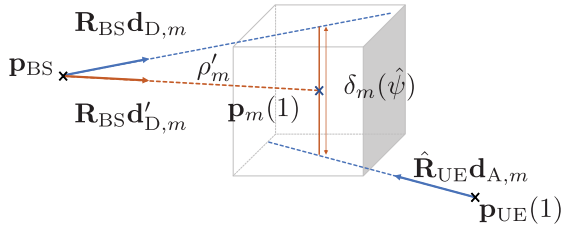

Fig. 4. Visualization of auxiliary direction $\mathbf{d}'_{\mathrm{D},m}$ and auxiliary points $\mathbf{p}_{\mathrm{UE}}(1)$ and $\mathbf{p}_m(1)$ in the scaled geometric model.

$$\mathbf{p}_m(r = 1) = \mathbf{A}_m^{-1} \mathbf{b}_m, \tag{26a}$$

$$\mathbf{A}_m = \mathbf{P}_{\perp}(\mathbf{R}_{\mathrm{BS}} \mathbf{d}_{\mathrm{D},m}) + \mathbf{P}_{\perp}(\hat{\mathbf{R}}_{\mathrm{UE}} \mathbf{d}_{\mathrm{A},m}), \tag{26b}$$

$$\mathbf{b}_m = \mathbf{P}_{\perp}(\mathbf{R}_{\mathrm{BS}} \mathbf{d}_{\mathrm{D},m}) \mathbf{p}_{\mathrm{BS}} + \mathbf{P}_{\perp}(\hat{\mathbf{R}}_{\mathrm{UE}} \mathbf{d}_{\mathrm{A},m}) \mathbf{p}_{\mathrm{UE}}(1) \tag{26c}$$

where $\mathbf{P}_{\perp}(\mathbf{d}) \triangleq \mathbf{I} - \mathbf{d}\mathbf{d}^{\mathsf{T}}$ is the projector onto the subspace orthogonal to the one spanned by a vector $\mathbf{d}$ (see Appendix C). Then, we define the auxiliary departure direction $\mathbf{d}'_{\mathrm{D},m}$ towards $\mathbf{p}_m(1)$ (in BS coordinate frame), and the corresponding distance ρ'_m as (see Fig. 4)

$$\mathbf{d}'_{\mathrm{D},m} = \mathbf{R}_{\mathrm{BS}}^{\mathsf{T}} \frac{\mathbf{p}_m(1) - \mathbf{p}_{\mathrm{BS}}}{\|\mathbf{p}_m(1) - \mathbf{p}_{\mathrm{BS}}\|}, \tag{27a}$$

$$\rho'_m = \|\mathbf{p}_m(1) - \mathbf{p}_{\mathrm{BS}}\|, \tag{27b}$$

allowing us to express $\mathbf{p}_m(1) = \mathbf{p}_{\mathrm{BS}} + \rho'_m \mathbf{R}_{\mathrm{BS}} \mathbf{d}'_{\mathrm{D},m}$.

What remains is to find ρ_0, since, with knowledge of ρ_0, we can scale the UE and IP positions to their correct place, keeping the BS fixed. To see this, consider triangles with the vertices $\{\mathbf{p}_{\mathrm{BS}}, \mathbf{p}_{\mathrm{UE}}(1), \mathbf{p}_m(1)\}$, $m > 1$, and scale them by ρ_0, yielding

$$\mathbf{p}_m(\rho_0) = \mathbf{p}_{\mathrm{BS}} + \rho_0 \rho'_m \mathbf{R}_{\mathrm{BS}} \mathbf{d}'_{\mathrm{D},m} \tag{28}$$

$$\mathbf{p}_{\mathrm{UE}}(\rho_0) = \mathbf{p}_{\mathrm{BS}} + \frac{\rho_0}{\rho_0} \rho_0 \mathbf{R}_{\mathrm{BS}} \mathbf{d}_{\mathrm{D},0}. \tag{29}$$

To recover the value of ρ_0, we rely on the TDoA measurements. Introducing $\boldsymbol{\Delta} = [\Delta_1, \ldots, \Delta_M]^{\mathsf{T}}$ with $\Delta_m = c(\tau_m - \tau_0)$, and $\tilde{\boldsymbol{\Delta}}(\rho_0) = [\tilde{\Delta}_1(\rho_0), \ldots, \tilde{\Delta}_M(\rho_0)]^{\mathsf{T}}$, where

$$\begin{aligned} \tilde{\Delta}_m(\rho_0) &= \|\mathbf{p}_m(\rho_0) - \mathbf{p}_{\mathrm{BS}}\| + \|\mathbf{p}_{\mathrm{UE}}(\rho_0) - \mathbf{p}_m(\rho_0)\| - \rho_0 \\ &= \rho_0(\rho'_m + \|\mathbf{d}_{\mathrm{D},0} - \rho'_m \mathbf{d}'_{\mathrm{D},m}\| - 1), \end{aligned} \tag{30}$$

allows us to formulate

$$\hat{\rho}_0 = \arg \min_{\rho_0} \|\boldsymbol{\Delta} - \tilde{\boldsymbol{\Delta}}(\rho_0)\|^2. \tag{31}$$

Since $\tilde{\boldsymbol{\Delta}}(\rho_0) = \rho_0 \boldsymbol{\beta}$ where $\beta_m = \rho'_m + \|\mathbf{d}_{\mathrm{D},0} - \rho'_m \mathbf{d}'_{\mathrm{D},m}\| - 1$, the optimization (31) is quadratic in ρ_0 and gives the closed-form solution $\hat{\rho}_0 = \boldsymbol{\beta}^{\mathsf{T}} \boldsymbol{\Delta} / \boldsymbol{\beta}^{\mathsf{T}} \boldsymbol{\beta}$. Note that $\beta_m \geq 0$ since $\tilde{\Delta}_m(\rho_0) \geq 0$, $\forall \rho_0$, according to the Triangle inequality. Hence, $\hat{\rho}_0 \geq 0$, and the solution is meaningful. The estimates of positions are then given by $\hat{\mathbf{p}}_{\mathrm{UE}} = \mathbf{p}_{\mathrm{UE}}(\hat{\rho}_0)$ and $\hat{\mathbf{p}}_m = \mathbf{p}_m(\hat{\rho}_0)$, $m = 1, \ldots, M$.

C. Step 3: Estimation of Clock Bias

After estimating the positions for UE and incidence points, we estimate the clock bias as

$$\hat{b} = \arg\min_{b} \|\boldsymbol{\tau} - \hat{\boldsymbol{\tau}}(\hat{\rho}_0) + b\mathbf{1}_{M+1}\|^2, \tag{32}$$

with $\boldsymbol{\tau} = [\tau_0, \ldots, \tau_M]^\mathsf{T}$, $\hat{\boldsymbol{\tau}}(\hat{\rho}_0) = [\hat{\tau}_0(\hat{\rho}_0), \ldots, \hat{\tau}_M(\hat{\rho}_0)]^\mathsf{T}$, and

$$\hat{\tau}_m(\hat{\rho}_0) = \begin{cases} \|\hat{\mathbf{p}}_{\text{UE}} - \mathbf{p}_{\text{BS}}\|/c = \hat{\rho}_0/c & m = 0 \\ (\|\hat{\mathbf{p}}_m - \mathbf{p}_{\text{BS}}\| + \|\hat{\mathbf{p}}_{\text{UE}} - \hat{\mathbf{p}}_m\|)/c & m \neq 0, \end{cases}$$

giving the closed-form solution $\hat{b} = \mathbf{1}^\mathsf{T}(\boldsymbol{\tau} - \hat{\boldsymbol{\tau}}(\hat{\rho}_0))/(M+1)$.

V. Fisher Information Analysis

In this section, we derive the FIM of the channel parameters and the localization parameters, and obtain the error bounds for 6D localization, mapping, as well as UE synchronization.

A. FIM of Channel Parameters

We define the vector of channel parameters as

$$\boldsymbol{\eta}_{\text{ch}} \triangleq [\underbrace{\boldsymbol{\theta}_{\text{A}}^\mathsf{T}, \boldsymbol{\theta}_{\text{D}}^\mathsf{T}, \boldsymbol{\tau}^\mathsf{T}}_{\boldsymbol{\eta} \in \mathbb{R}^{5(M+1)}}, \mathbf{h}_{\text{R}}^\mathsf{T}, \mathbf{h}_{\text{I}}^\mathsf{T}]^\mathsf{T} \in \mathbb{R}^{7(M+1)}, \tag{33}$$

where $\mathbf{h}_{\text{R}} = [h_{\text{R},0}, \ldots, h_{\text{R},M}]^\mathsf{T}$, and $\mathbf{h}_{\text{I}} = [h_{\text{I},0}, \ldots, h_{\text{I},M}]^\mathsf{T}$. The FIM of $\boldsymbol{\eta}_{\text{ch}}$, considering the signal model (1), is given by the Slepian-Bangs formula [53, Section 3.9] as

$$[\mathbf{J}_{\boldsymbol{\eta}_{\text{ch}}}]_{i,j} = \frac{2E_{\text{s}}}{N_0} \sum_{k=1}^{K} \sum_{n=1}^{N} \Re\left\{ \frac{\partial \widetilde{y}_{k,n}}{\partial [\boldsymbol{\eta}_{\text{ch}}]_i}^{\mathsf{H}} \frac{\partial \widetilde{y}_{k,n}}{\partial [\boldsymbol{\eta}_{\text{ch}}]_j} \right\}, \tag{34}$$

where $\widetilde{y}_{k,n}$ is the noise-free part of the observation $y_{k,n}$, and the gradients can be found in [16, Appendix. I]. Then we obtain the equivalent Fisher information matrix (EFIM) of AoAs, AoDs, and ToAs as in the following:

$$\mathbf{J}_{\boldsymbol{\eta}} = \left[[\mathbf{J}_{\boldsymbol{\eta}_{\text{ch}}}^{-1}]_{1:5(M+1),1:5(M+1)} \right]^{-1}. \tag{35}$$

B. FIM of Localization Parameters

Expressing $\mathbf{R}_{\text{UE}} = [\mathbf{r}_{\text{UE},1}, \mathbf{r}_{\text{UE},2}, \mathbf{r}_{\text{UE},3}]$ with $\mathbf{r}_{\text{UE},1}$, $\mathbf{r}_{\text{UE},2}$, and $\mathbf{r}_{\text{UE},3}$ as columns, we recall the vector of localization unknowns as

$$\boldsymbol{\xi} = [\mathbf{r}^\mathsf{T}, \mathbf{p}_{\text{UE}}^\mathsf{T}, \mathbf{p}_1^\mathsf{T}, \ldots, \mathbf{p}_M^\mathsf{T}, b]^\mathsf{T} \in \mathbb{R}^{3(M+1)+10}. \tag{36}$$

where $\mathbf{r} = \text{vec}(\mathbf{R}_{\text{UE}}) = [\mathbf{r}_{\text{UE},1}^\mathsf{T}, \mathbf{r}_{\text{UE},2}^\mathsf{T}, \mathbf{r}_{\text{UE},3}^\mathsf{T}]^\mathsf{T}$. Then we obtain the FIM $\mathbf{J}_{\boldsymbol{\xi}}$ by transforming the channel parameters to localization parameters through the Jacobian matrix $\boldsymbol{\Upsilon}$ as follows [53, Eq. (3.30)]:

$$\mathbf{J}_{\boldsymbol{\xi}} = \boldsymbol{\Upsilon}^\mathsf{T} \mathbf{J}_{\boldsymbol{\eta}} \boldsymbol{\Upsilon}, \tag{37}$$

where $[\boldsymbol{\Upsilon}]_{i,j} = \partial [\mathbf{J}_{\boldsymbol{\eta}}]_i / \partial [\mathbf{J}_{\boldsymbol{\xi}}]_j$, and $\mathbf{J}_{\boldsymbol{\eta}}$ is given in (35). To obtain the elements of the transformation matrix $\boldsymbol{\Upsilon}$, we need the derivatives of channel parameters w.r.t. localization parameters, which are obtained in Appendix A. We note that $\partial [\boldsymbol{\eta}]_i / \partial \mathbf{r} = \text{vec}(\partial [\boldsymbol{\eta}]_i / \partial \mathbf{R}_{\text{UE}})$.

To obtain the error bounds, we need to account for the constraint that $\mathbf{R}_{\text{UE}} \in \text{SO}(3)$. We obtain the constrained Cramér-Rao bound (CCRB) [54] giving the lower bound on the estimation error covariance, for any unbiased estimator subject to the required constraint on $\mathbf{R}_{\text{UE}}$. The set of constraints to be satisfied due to orthogonality of the rotation matrix (i.e., $\mathbf{R}_{\text{UE}}^\mathsf{T}\mathbf{R}_{\text{UE}} = \mathbf{I}_3$) is given by

$$\begin{aligned} \mathbf{h}(\boldsymbol{\xi}) = [&\|\mathbf{r}_1\|^2 - 1, \mathbf{r}_2^\mathsf{T}\mathbf{r}_1, \mathbf{r}_3^\mathsf{T}\mathbf{r}_1, \\ &\|\mathbf{r}_2\|^2 - 1, \mathbf{r}_2^\mathsf{T}\mathbf{r}_3, \|\mathbf{r}_3\|^2 - 1]^\mathsf{T} = \mathbf{0}_6. \end{aligned} \tag{38}$$

Considering $\mathbf{M} = \text{blkdiag}(\frac{1}{\sqrt{2}}\mathbf{M}_0, \mathbf{I}_{3(M+1)+1})$ with

$$\mathbf{M}_0 = \begin{bmatrix} -\mathbf{r}_3 & \mathbf{0}_3 & \mathbf{r}_2 \\ \mathbf{0}_3 & -\mathbf{r}_3 & -\mathbf{r}_1 \\ \mathbf{r}_1 & \mathbf{r}_2 & \mathbf{0}_3 \end{bmatrix} \in \mathbb{R}^{9\times 3}, \tag{39}$$

meets $\mathbf{G}(\boldsymbol{\xi})\mathbf{M} = \mathbf{0}$ where $[\mathbf{G}(\boldsymbol{\xi})]_{i,j} = \partial [\mathbf{h}(\boldsymbol{\xi})]_i / \partial [\boldsymbol{\xi}]_j$, and gives [54]

$$\mathbf{C}_{\boldsymbol{\xi}}^{(\text{CCRB})} = \mathbf{M}(\mathbf{M}^\mathsf{T}\mathbf{J}_{\boldsymbol{\xi}}\mathbf{M})^{-1}\mathbf{M}^\mathsf{T}, \tag{40}$$

in which $\mathbf{J}_{\boldsymbol{\xi}}$ is given in (37). Then any unbiased estimate $\hat{\boldsymbol{\xi}}$ subject to $\hat{\mathbf{R}}_{\text{UE}} \in \text{SO}(3)$ satisfies $\mathbb{E}\{(\hat{\boldsymbol{\xi}} - \boldsymbol{\xi})(\hat{\boldsymbol{\xi}} - \boldsymbol{\xi})^\mathsf{T}\} \succeq \mathbf{C}_{\boldsymbol{\xi}}^{(\text{CCRB})}$, where the expectation is with respect to the noise.

Finally, we define orientation error bound (OEB), position error bound (PEB), IPs error bound (IPEB), and synchronization error bound (SEB), which show the lower bound on the RMSE of estimation as

$$\text{OEB} = \left[\text{tr}\left(\mathbf{C}_{\mathbf{R}_{\text{UE}}}\right)\right]^{\frac{1}{2}}, \qquad \text{PEB} = \left[\text{tr}\left(\mathbf{C}_{\mathbf{p}_{\text{UE}}}\right)\right]^{\frac{1}{2}},$$

$$\text{IPEB} = \left[\sum_{m=1}^{M} \text{tr}\left(\mathbf{C}_{\mathbf{p}_m}\right)/M\right]^{\frac{1}{2}}, \qquad \text{SEB} = \left[\text{tr}\left(\mathbf{C}_b\right)\right]^{\frac{1}{2}},$$

where $\mathbf{C}_{\mathbf{R}_{\text{UE}}}$, $\mathbf{C}_{\mathbf{p}_{\text{UE}}}$, $\mathbf{C}_{\mathbf{p}_m}$, and $\mathbf{C}_b$ are diagonal sub-matrices in $\mathbf{C}_{\boldsymbol{\xi}}^{(\text{CCRB})}$ corresponding to $\mathbf{r}$, $\mathbf{p}_{\text{UE}}$, $\mathbf{p}_m$, and b, respectively. We note that $\mathbf{C}_b$ is a scalar equal to the variance of clock bias estimation, and that the RMSE of estimation of $\mathbf{r}$ is equal to $\mathbb{E}\{\|\mathbf{r} - \hat{\mathbf{r}}\|^2\} = \mathbb{E}\{\|\mathbf{R}_{\text{UE}} - \hat{\mathbf{R}}_{\text{UE}}\|_{\text{F}}^2\}$. In addition, the IPEB (in meters) represents the RMSE of all the IP location estimates, and is a simplified form of the widely used GOSPA metric, from radar sensing and target tracking [55].

VI. Numerical Results

A. Simulation Setup

Our simulation scenario consists of an indoor environment shown in Fig. 5, where the BS is mounted vertically. We employ uniform planar arrays (UPAs) in both BS and UE, consisting of rectangular configurations of $\sqrt{N_{\text{BS}}} \times \sqrt{N_{\text{BS}}}$ and $\sqrt{N_{\text{UE}}} \times \sqrt{N_{\text{UE}}}$ antennas, with half-wavelength inter-element spacing. Assuming the configurations in the reference orientation where the planar arrays are parallel to the global XY-axes, facilitates expressing $\boldsymbol{\Delta}_{\text{BS}}$ and $\boldsymbol{\Delta}_{\text{UE}}$, i.e., the matrices containing the

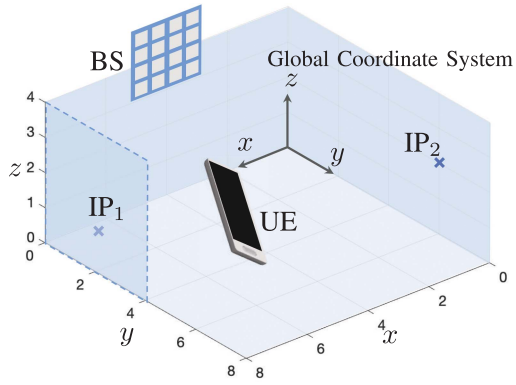

Fig. 5. The indoor scenario considered in simulations, with default parameters provided in Table II.

positions of antenna elements in local coordinate frames.[6] For the channel model, we correspond incidence points to reflecting surfaces with reflection coefficient Γ_{ref}.[7] We consider that the channel gains are proportional to the free-space path loss, with a random phase uniformly distributed in $[0, 2\pi)$, and account for the radiation pattern of antennas [56, Chapter 4] as follows:

$$|h_m|^2 = \begin{cases} \dfrac{\lambda^2 \cos^2\theta^{(\text{el})}_{\text{A},0} \cos^2\theta^{(\text{el})}_{\text{D},0}}{(4\pi)^2 \|\mathbf{p}_{\text{BS}} - \mathbf{p}_{\text{UE}}\|^2} & m = 0 \\ \dfrac{\lambda^2 \Gamma_{\text{ref}} \cos^2\theta^{(\text{el})}_{\text{A},m} \cos^2\theta^{(\text{el})}_{\text{D},m}}{(4\pi)^2 (\|\mathbf{p}_{\text{BS}} - \mathbf{p}_m\| + \|\mathbf{p}_{\text{UE}} - \mathbf{p}_m\|)^2} & m \neq 0. \end{cases}$$

The pilots are set to $x_{k,n} = \sqrt{E_s}$ and the components in precoding and combining vectors $\boldsymbol{f}_k$ and $\boldsymbol{w}_k$ are assumed to comprise unit-modulus elements with random phase, different for each OFDM symbol.

The rotation matrices are also generated with help of Euler angles $\alpha \in [0, 2\pi)$, $\beta \in [0, \pi)$, $\gamma \in [0, 2\pi)$ [39], using $\mathbf{R} = \mathbf{R}_z(\alpha)\mathbf{R}_y(\beta)\mathbf{R}_x(\gamma)$, where $\mathbf{R}_z(\alpha)$, $\mathbf{R}_y(\beta)$, and $\mathbf{R}_x(\gamma)$ are transformation matrices for counter-clockwise rotations around z, y, and x axes through α, β, and γ, respectively [39].

Table II lists all the default simulation parameters, where default orientation for UE is either of $\mathbf{R}_1$ or $\mathbf{R}_2$ given by

$$\mathbf{R}_1 = \mathbf{R}_z(\pi/6)\mathbf{R}_y(-\pi/4)\mathbf{R}_x(-\pi/36), \mathbf{R}_2 = \mathbf{R}_x(\pi/2). \tag{41}$$

In some cases, we generate the orientation randomly. More precisely, α, β, and γ are generated randomly. Although we note that this is not equivalent to uniform sampling of SO(3), it is an easy way to evaluate different orientations. Also, in some simulations, the positions of IPs are generated randomly, while the positions of default IPs labeled in Fig. 5 are given in

$$\mathbf{P} = [\mathbf{p}_1, \mathbf{p}_2] = \left[[8, 2, 1]^{\mathsf{T}}, [0, 6, 2]^{\mathsf{T}}\right]. \tag{42}$$

[6]The antenna element located at row i and column j of such configuration for BS, $1 \leq i, j \leq \sqrt{N_{\text{BS}}}$, is $(i-1)\sqrt{N_{\text{BS}}} + j$-th antenna, which is located at $\mathbf{x}_{\text{BS},(i-1)\sqrt{N_{\text{BS}}}+j} = [j - (\sqrt{N_{\text{BS}}}+1)/2, -i + (\sqrt{N_{\text{BS}}}+1)/2, 0]^{\mathsf{T}} d_{\text{BS}}$, with $d_{\text{BS}} = \lambda/2$. Similarly, we express the positions of antenna elements in UE array.

[7]For the specific IP_1 and IP_2, at the given positions $\mathbf{p}_1$ and $\mathbf{p}_2$, we assume $\Gamma_{\text{ref},1} = 0.2$ and $\Gamma_{\text{ref},2} = 0.8$, respectively. However, for the general IPs at random positions, $\Gamma_{\text{ref}} = 0.7$.

TABLE II
DEFAULT SIMULATION PARAMETERS. PARAMETERS THAT VARY ARE MARKED WITH $*$

Parameter	Symbol	Value
Propagation Speed	c	3×10^8 m/s
Carrier Frequency	f_c	28 GHz
Subcarrier Spacing	Δ_f	120 kHz
# Subcarriers*	N_f	3333
# OFDM Symbols	K	10
Transmit Power*	P_{TX}	10 dBm
Noise PSD	N_0	-174 dBm/Hz
UE Noise Figure	n_0	13 dB
BS # Antennas*	N_{BS}	64 (8×8)
UE # Antennas*	N_{UE}	4 (2×2)
BS Position	$\mathbf{p}_{\text{BS}}$	$[4, 0, 4]^{\mathsf{T}}$
BS Orientation	$\mathbf{R}_{\text{BS}}$	$\mathbf{R}_x(-\pi/2)$
UE Position*	$\mathbf{p}_{\text{UE}}$	$[5, 4, 1]^{\mathsf{T}}$
UE Orientation*	$\mathbf{R}_{\text{UE}}$	given in (41)
IP Positions*	$\mathbf{p}_m$	given in (42)
Reflection Coefficient*	Γ_{ref}	$[0.2, 0.8]$, 0.7
Clock Offset	b	100 ns
# Monte Carlo Simulations	N_s	1000

The simulations are done in MATLAB 2021b. For the optimization on manifolds, we utilize the Manopt toolbox [57].

B. Obtaining the Likelihood Parameters

To obtain the parameters $\boldsymbol{\kappa}_{\text{A}}$, $\boldsymbol{\kappa}_{\text{D}}$, and $\Sigma_{\boldsymbol{\tau}}$ presented in Section III, considering the independence of angles and delays, we derive the covariance matrix

$$\mathbf{C}_{\boldsymbol{\eta}} = \text{diag}\left(\mathbf{J}_{\boldsymbol{\eta}}^{-1}\right) = \text{blkdiag}(\mathbf{C}_{\boldsymbol{\theta}_{\text{A}}}, \mathbf{C}_{\boldsymbol{\theta}_{\text{D}}}, \mathbf{C}_{\boldsymbol{\tau}}), \tag{43}$$

where $\mathbf{C}_{\boldsymbol{\theta}_{\text{A}}}$, $\mathbf{C}_{\boldsymbol{\theta}_{\text{D}}}$ and $\mathbf{C}_{\boldsymbol{\tau}}$ are diagonal matrices corresponding to AoAs, AoDs, and ToAs, respectively. Furthermore, using the independence assumption, FIMs of $\boldsymbol{\theta}_{\text{A}}$ and $\boldsymbol{\theta}_{\text{D}}$ are given, with respect to $\boldsymbol{\kappa}_{\text{A}}$ and $\boldsymbol{\kappa}_{\text{D}}$, respectively, by [22]

$$\mathbf{J}_{\boldsymbol{\theta}_{\text{A}}} = \text{diag}\left(\boldsymbol{\kappa}_{\text{A}} \odot I_1(\boldsymbol{\kappa}_{\text{A}}) \oslash I_0(\boldsymbol{\kappa}_{\text{A}})\right), \tag{44a}$$

$$\mathbf{J}_{\boldsymbol{\theta}_{\text{D}}} = \text{diag}\left(\boldsymbol{\kappa}_{\text{D}} \odot I_1(\boldsymbol{\kappa}_{\text{D}}) \oslash I_0(\boldsymbol{\kappa}_{\text{D}})\right), \tag{44b}$$

where $I_1(\cdot)$ is the modified Bessel function of order 1. Solving the above equations gives $\boldsymbol{\kappa}_{\text{A}}$ and $\boldsymbol{\kappa}_{\text{D}}$.[8] Obviously, $\Sigma_{\boldsymbol{\tau}} = \mathbf{C}_{\boldsymbol{\tau}}$.

In order to motivate removing dependencies, we evaluate the CDF of PEB with and without the independence assumption, using $N_s = 1000$ Monte Carlo simulations. In every simulation, we randomize $\mathbf{R}_{\text{UE}}$ as well as $\mathbf{p}_{\text{UE}}$, $\mathbf{p}_1, \ldots, \mathbf{p}_M \in [0, 8] \times [0, 8] \times [0, 4]\,\text{m}^3$. Then we obtain the PEB in two cases: the general case using $\mathbf{J}_{\boldsymbol{\eta}}$ in (37) and then (40); the independent case, with $\mathbf{J}_{\boldsymbol{\eta}}^{\text{ind}} = (\text{diag}(\mathbf{J}_{\boldsymbol{\eta}}^{-1}))^{-1}$ in (37) and then (40). The CDF curves are shown for three different numbers of IPs, i.e., $M \in \{1, 2, 10\}$. As seen in Fig. 6, the distribution of PEB with the independence of channel parameters is closely following that of the general case, meaning that not only the angles and delays of different paths but also the azimuth and elevation angles of every individual path can be taken to be independent without a considerable impact. Similar observations hold for the other bounds, i.e., OEB, IPEB, and SEB. Although in certain cases the

[8]Specially in high SNR regimes, the values in $\boldsymbol{\kappa}_{\text{A}}$ and $\boldsymbol{\kappa}_{\text{D}}$ are large, and therefore, $I_1(\boldsymbol{\kappa}_{\text{A}}) \oslash I_0(\boldsymbol{\kappa}_{\text{A}}) \to \mathbf{1}_{2(M+1)}$ and $I_1(\boldsymbol{\kappa}_{\text{D}}) \oslash I_0(\boldsymbol{\kappa}_{\text{D}}) \to \mathbf{1}_{2(M+1)}$, leading to $\boldsymbol{\kappa}_{\text{A}} = \text{diag}(\mathbf{C}_{\boldsymbol{\theta}_{\text{A}}}^{-1})$ and $\boldsymbol{\kappa}_{\text{D}} = \text{diag}(\mathbf{C}_{\boldsymbol{\theta}_{\text{D}}}^{-1})$. There are other approximations for the ratio $I_1(x)/I_0(x)$, for example [58, Lemma 2].

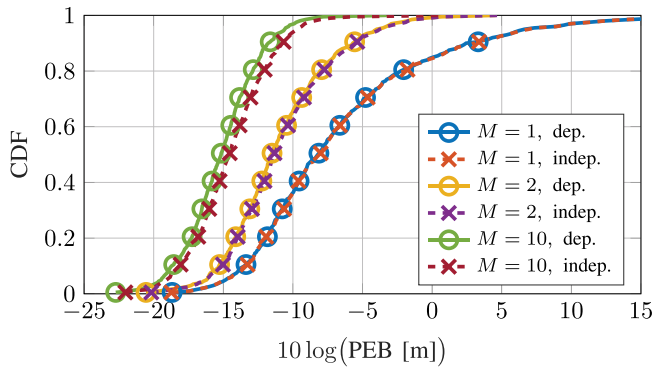

Fig. 6. cumulative distribution function (CDF) of PEB with and without independence of channel parameters for a varying number of incidence points.

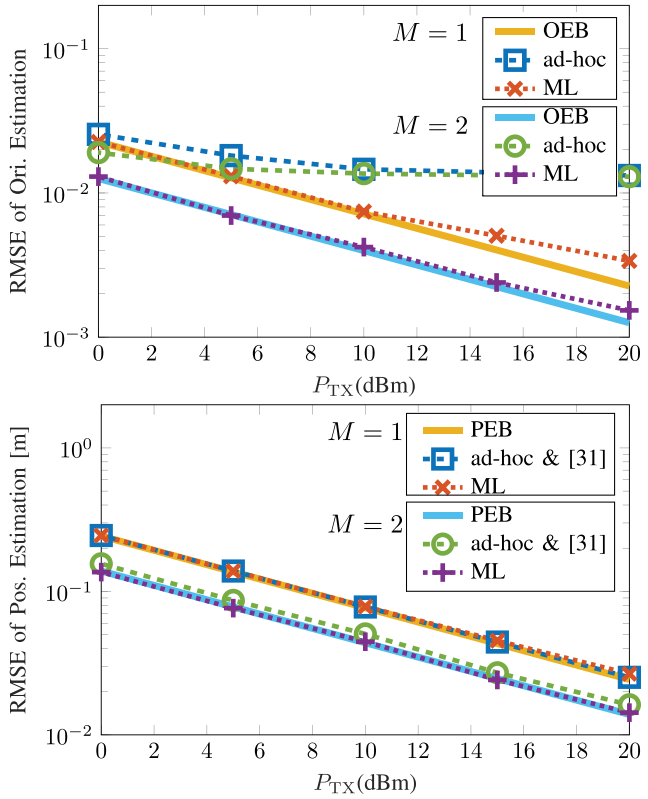

Fig. 7. RMSE of UE orientation estimation (top) and UE position estimation (bottom) vs. P_{TX}, for ML and ad-hoc estimators, with search granularity $\pi/200$, for $M \in \{1, 2\}$, with $\mathbf{R}_{\text{UE}} = \mathbf{R}_2$ and the default $\mathbf{p}_{\text{UE}}$, $\mathbf{p}_1$, and $\mathbf{p}_2$ (in case of $M = 2$). The figures also include the OEB and PEB.

performance with dependencies can differ significantly (up to 50%) from the independent case, the effect is limited on average.

C. Results and Discussions

1) Performance Evaluation of ML and Ad-Hoc Estimators: The performance evaluation for the proposed estimators is shown in Fig. 7, where we show the RMSE of UE orientation and position estimation vs. the transmit power P_{TX}, for two cases, i.e., $M = 1$ with IP_1, and $M = 2$, with both IP_1 and IP_2, with the reflection coefficients $\Gamma_{\text{ref},1} = 0.2$ for IP_1, and $\Gamma_{\text{ref},2} = 0.8$ for IP_2. We observe that the performance of both estimators improves by increasing the transmit power, closely following the corresponding bounds. Specifically, the RMSE of UE position estimation using the proposed ad-hoc routine sees a negligible gap compared to the CRB, for a large range of transmit powers. This of course depends on the geometry as well as the granularity of the 1-dimensional search for obtaining ψ. Not surprisingly, in the low SNR regimes, the performance deviates from the bound, but in the case of $M = 2$, the ML estimator is able to reduce the gap. This gap is due to the ignorance of the distribution of measurements in the ad-hoc estimator, and it is especially pronounced in unfavorable positions of UE, where the quality of different paths arriving at UE are remarkably different. In moderate SNR, the ML estimation yields an RMSEs close to the performance bounds. In very high SNR regimes, the performance of the ad-hoc estimator saturates due to the granularity of angle search. It is then refined using the ML, and the gap to the bounds is substantially reduced. As a benchmark, we compare the positioning performance of the ad-hoc estimator to that of the only other available estimator, i.e., [31, eq. (15)–(16)]. We observe that the proposed ad-hoc estimator achieves identical performance. The strength of [31] is that it does not require an estimate of the rotation matrix for estimating the UE position, but at the same time, the one-dimensional search of our method for estimation of rotation matrix should be done anyway, to initialize the ML algorithm. The tightness of ML estimator to the CRB, and the negligible gap between the performance of the ad-hoc estimator and the lower bounds for a practical range, shows the efficiency of our proposed estimation algorithms.

2) Impact of System Parameters: In Fig. 8, we evaluate the impact of bandwidth, the number of antennas, and the number of IPs, using $\mathbf{R}_{\text{UE}} = \mathbf{R}_1$ and the default $\mathbf{p}_{\text{UE}}$. For evaluation of the impact of bandwidth and number of antennas, we consider one IP at the default position $\mathbf{p}_1$, while we evaluate the impact of the number of IPs, in an average sense, i.e., the positions of IPs are randomized, and the average error bounds are obtained.

As it is observed in the left plot in Fig. 8, increasing the bandwidth, which leads to higher ToA accuracy and improved delay resolution, decreases the error bounds. This trend, however, saturates at some point ($\approx$ 100 MHz), because further improvement is limited by the accuracy of angle measurements. The OEB is the least benefited from the enhancement of ToA accuracy, which makes sense since the orientation is determined mainly by angle measurements and not the delays.

The two middle plots of Fig. 8, show the performance gains achieved when the angular resolution and accuracy improve thanks to an increase in the number of UE and BS antennas. PEB and SEB benefit most from additional UE antennas, while IPEB benefits most from additional BS antennas. Since analog combining is used with a fixed number of precoders and combiners, there is no array gain, which leads again to saturation at a larger number of antennas, when there are no further resolution gains, and the performance is limited by the bandwidth.

Finally, in the right plot of Fig. 8 we show the impact of the number of IPs. We see that increasing number of IPs leads to improvements in the OEB, PEB, and SEB. The reduction of

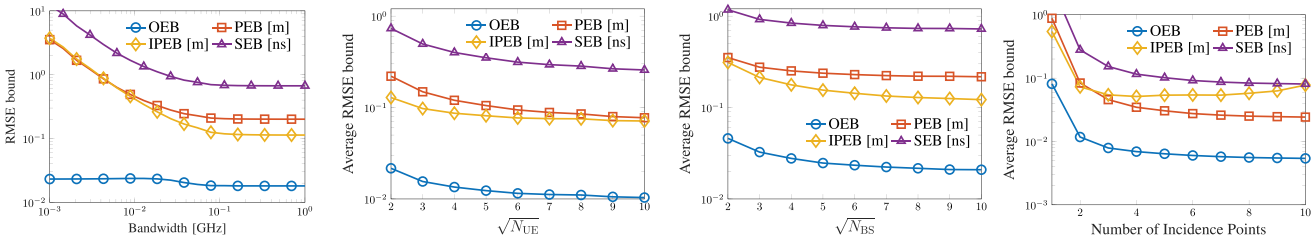

Fig. 8. Impact of bandwidth (left), number of UE antennas (middle-left), number of BS antennas (middle-right), and number of IPs (right) on (average) performance error bounds.

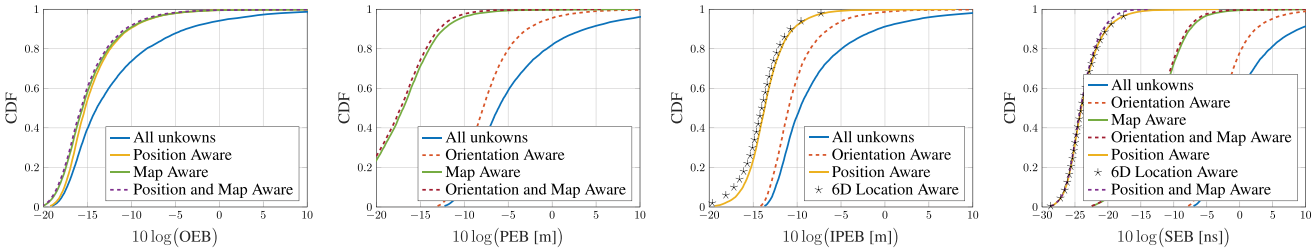

Fig. 9. CDF of OEB (left), PEB (middle-left), IPEB (middle-right), and SEB (right), under different levels of side-information. The position and orientation of UE are randomized, and the default IP_1 is included.

error bounds is especially considerable when the number of IPs changes from 1 to 2. The reason is that, when $M = 1$, the quality of estimating AoA or AoD degrades in certain positions, and this causes larger error bounds, on average. However, when another IP is added, the probability of having both IPs at unfavorable positions reduces significantly, and the average error bounds decrease. For the IPEB, while it decreases at the beginning with the number of incidence points, it may experience small fluctuations or even increase at larger M. This is due to the increase in the number of unknowns, i.e., positions of IPs.

3) Impact of Known Parameters: In this part, we assess the impact of known parameters, i.e., we evaluate the best achievable estimation accuracy, if some of the parameters are known. For that, we depict the CDF of error bounds in Fig. 9. To set up the Monte Carlo simulations, we consider only one IP at the default position $\mathbf{p}_1$, while we randomize $[p_{\text{UE},x}, p_{\text{UE},y}] \in [0, 8] \times [0, 8]$ in the $p_{\text{UE},z} = 1$ plane (though $p_{\text{UE},z} = 1$ is considered unknown), as well as the UE orientation. The CDF curves are shown for $N_s = 10,000$ realizations. In terms of the OEB, position knowledge of either the UE or IP improves the orientation accuracy, congruent with the findings from [22] with 2 BSs. In terms of the PEB, orientation awareness is less important than the knowledge from the mapping, i.e., the position of the incidence point. Similarly, the knowledge of UE position can help mapping, and certainly, if both $\mathbf{p}_{\text{UE}}$ are $\mathbf{R}_{\text{UE}}$ are known, lower IPEB is achieved. Finally, in terms of the SEB, a variety of cases exist, with and without side information from either or some of $\mathbf{R}_{\text{UE}}$, $\mathbf{p}_{\text{UE}}$, and $\mathbf{p}_1$. As we have seen on the other bounds, knowledge of orientation is the least informative, and the UE and IP location awareness provide a large amount of information on the clock bias.

4) 6D Localization Coverage: As the last step in our simulations, we evaluate the localization coverage and performance

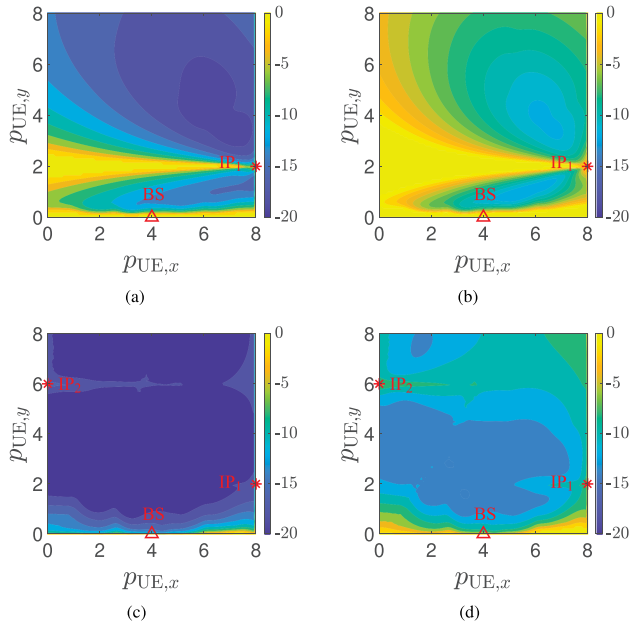

Fig. 10. Contour plots of (a) OEB, (b) PEB [m] with IP_1; (c) OEB, (d) PEB [m] with IP_1 and IP_2, for $p_{\text{UE},z} = 1$, $\mathbf{R}_{\text{UE}} = \mathbf{R}_2$.

robustness, via contour plots of OEB and PEB, in the region around the BS and IPs. Fig. 10 shows the contour plots of error bounds, when x and y coordinates of UE position are varied, while the z coordinate is fixed to 1, considering 1 NLoS path (top row) or 2 NLoS paths (bottom row). As the UE gets closer to the IP (which has the lower channel gain compared to the direct path from the BS), the quality of estimation of all parameters improves, unless if UE approaches the $y = 0$ plane resulting in $\theta_{\text{D},0}^{(\text{el})}$ close to $\pi/2$, which in turn strongly attenuates the LoS

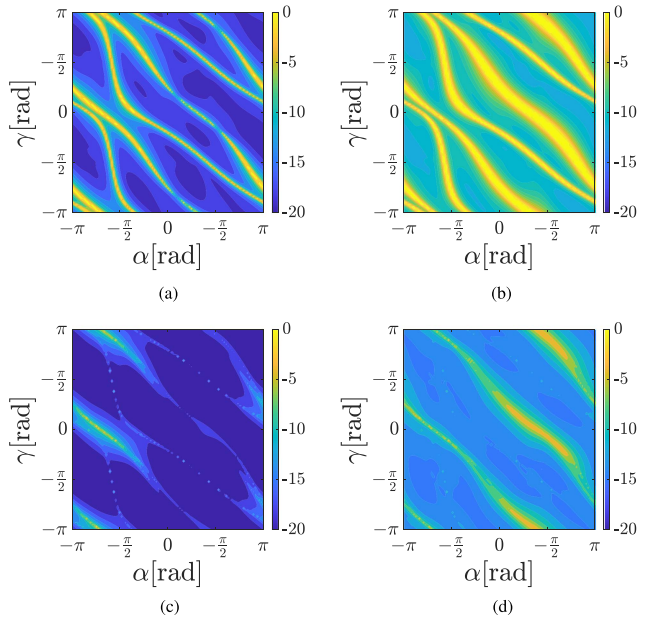

Fig. 11. Contour plots of of (a) OEB, (b) PEB [m] with IP_1; (c) OEB, (d) PEB [m] with IP_1 and IP_2, for $\beta = -\pi/4$.

path, degrades the estimation of $\boldsymbol{\theta}_{\text{D},0}$, and accordingly increases the error. Including IP_2 at the default position provides another signal source and improves the coverage. In summary, good performance is achieved close to IPs, with a graceful degradation further away. However, if the UE should not be so close to the IP that the NLoS paths is no longer resolvable from the LoS path.

In a similar fashion, we depict the contour plots of error bounds, for a range of rotation angles of UE in Fig. 11, by fixing one of the Euler angles $\beta = -\pi/4$. If only IP_1 is present, we observe a continuous set of orientations for which the bounds are infinite. Specifically, the orientation caused by the composition of rotations around z and x axes through α and γ respectively, results in the received ray from either LoS or NLoS paths to hit the UE antenna array on the endfire, and does not provide a high-quality estimation of either of AoAs. Subsequently, both OEB and PEB are affected. However, once these specific orientations change, the signal arrives in more appropriate directions, and the bounds improve. Once a second IP is added, the problem is non-identifiable for only a reduced set of configurations. Hence, with $M > 1$ NLoS paths, a more uniform 6D localization coverage can be achieved.

While not shown, the performance as a function of the IP location can also be evaluated. With a single IP, the bounds become infinite when the IP is on the 3D line between BS and UE, which is a very unlikely configuration.

VII. Conclusion

In this paper, we considered a single BS transmitting a mmWave OFDM signal and a multi-antenna UE receiving the LoS path and at least one resolvable NLoS path. The objective was to solve the snapshot 6D localization problem whereby the 3D position, the 3D orientation, and the clock bias of the UE have to be estimated, as well as the positions of the incidence points. Two estimation routines, namely ML estimation (which is a high-dimensional non-convex optimization problem over a product of manifolds) and an ad-hoc routine, were applied and their performance was evaluated. Although the performance of the former attains the CRB, the latter provides estimates based on geometrical arguments. These estimates closely follow the CRB for a large transmit power range, and serve as initialization to the recursive algorithms for solving the ML complex estimation problem. In contrast, the proposed ad-hoc solution reduces the complexity to a single 1-dimensional search over a finite interval, combined with closed-form expressions. After obtaining an efficient ML-based estimator, we evaluated the impact of different parameters, such as bandwidth, number of antennas, number of NLoS paths, etc., through evaluation of CRB. These results indicate that at least 2 NLoS paths are needed to render the problem identifiable for most geometric configurations.

There are several possible extensions of the current work, which may be addressed in future studies. First of all, a solution to the obstructed LoS scenarios should be developed. Secondly, besides single-bounce NLoS paths, there may double- and multiple-bounce reflections, and the performance of localization in these conditions should be investigated.

Appendix A
Partial Derivatives of AoAs, AoDs, and ToAs w.r.t. Localization Parameters

A. Auxiliary Variables

We define auxiliary variables

$$\mathbf{u}_{\text{A},m\neq 0} = \frac{\mathbf{p}_m - \mathbf{p}_{\text{UE}}}{\|\mathbf{p}_m - \mathbf{p}_{\text{UE}}\|}, \quad \mathbf{u}_{\text{A},0} = \frac{\mathbf{p}_{\text{BS}} - \mathbf{p}_{\text{UE}}}{\|\mathbf{p}_{\text{BS}} - \mathbf{p}_{\text{UE}}\|}, \tag{45a}$$

$$\mathbf{u}_{\text{D},m\neq 0} = \frac{\mathbf{p}_m - \mathbf{p}_{\text{BS}}}{\|\mathbf{p}_m - \mathbf{p}_{\text{BS}}\|}, \quad \mathbf{u}_{\text{D},0} = \frac{\mathbf{p}_{\text{UE}} - \mathbf{p}_{\text{BS}}}{\|\mathbf{p}_{\text{UE}} - \mathbf{p}_{\text{BS}}\|}, \tag{45b}$$

as well as $\mathbf{u}_1 = [1,0,0]^{\mathsf{T}}$, $\mathbf{u}_2 = [0,1,0]^{\mathsf{T}}$, and $\mathbf{u}_3 = [0,0,1]^{\mathsf{T}}$, for later use. Considering $\mathbf{R}_{\text{UE}} = [\mathbf{r}_{\text{UE},1}, \mathbf{r}_{\text{UE},2}, \mathbf{r}_{\text{UE},3}]$ and $\mathbf{R}_{\text{BS}} = [\mathbf{r}_{\text{BS},1}, \mathbf{r}_{\text{BS},2}, \mathbf{r}_{\text{BS},3}]$ gives $\mathbf{R}_{\text{UE}}\mathbf{u}_i = \mathbf{r}_{\text{UE},i}$ and $\mathbf{R}_{\text{BS}}\mathbf{u}_i = \mathbf{r}_{\text{BS},i}$, $i = 1,2,3$.

B. Mathematical Identities

The following mathematical identities are used in obtaining the derivatives:

$$\frac{\partial}{\partial \mathbf{x}} \mathbf{a}^{\mathsf{T}}\mathbf{x}^{\mathsf{T}}\mathbf{b} = \mathbf{b}\mathbf{a}^{\mathsf{T}}, \tag{46a}$$

$$\frac{\partial}{\partial \mathbf{x}} \mathbf{a}^{\mathsf{T}}\mathbf{x} = \mathbf{a}, \tag{46b}$$

$$\frac{\partial}{\partial \mathbf{x}} \text{acos}(v(\mathbf{x})) = -\frac{1}{\sqrt{1-v^2(\mathbf{x})}} \frac{\partial v(\mathbf{x})}{\partial \mathbf{x}}, \tag{46c}$$

$$\frac{\partial}{\partial \mathbf{x}} \text{atan2}(v(\mathbf{x}), w(\mathbf{x})) = \frac{w(\mathbf{x})\frac{\partial v(\mathbf{x})}{\partial \mathbf{x}} - v(\mathbf{x})\frac{\partial w(\mathbf{x})}{\partial \mathbf{x}}}{v^2(\mathbf{x}) + w^2(\mathbf{x})}, \tag{46d}$$

$$\frac{\partial}{\partial \mathbf{x}} \frac{\mathbf{x}-\mathbf{a}}{\|\mathbf{x}-\mathbf{a}\|} = \frac{\mathbf{I}}{\|\mathbf{x}-\mathbf{a}\|} - \frac{(\mathbf{x}-\mathbf{a})(\mathbf{x}-\mathbf{a})^{\mathsf{T}}}{\|\mathbf{x}-\mathbf{a}\|^3}, \tag{46e}$$

$$\frac{\partial}{\partial \mathbf{x}}\|\mathbf{x}-\mathbf{a}\| = \frac{\mathbf{x}-\mathbf{a}}{\|\mathbf{x}-\mathbf{a}\|}. \tag{46f}$$

In (46c) and (46d), if the derivatives are taken with respect to a matrix, we replace $\mathbf{x}$ by $\mathbf{x}$, and the equations still hold.

C. Reformulation of AoAs and AoDs

Using the defined auxiliary variables, one can express

$$\boldsymbol{\theta}_{\mathrm{A},m} = [\mathrm{atan2}(\mathbf{r}_{\mathrm{UE},2}^{\mathsf{T}}\mathbf{u}_{\mathrm{A},m}, \mathbf{r}_{\mathrm{UE},1}^{\mathsf{T}}\mathbf{u}_{\mathrm{A},m}), \mathrm{acos}(\mathbf{r}_{\mathrm{UE},3}^{\mathsf{T}}\mathbf{u}_{\mathrm{A},m})]^{\mathsf{T}},$$

$$\boldsymbol{\theta}_{\mathrm{D},m} = [\mathrm{atan2}(\mathbf{r}_{\mathrm{BS},2}^{\mathsf{T}}\mathbf{u}_{\mathrm{D},m}, \mathbf{r}_{\mathrm{BS},1}^{\mathsf{T}}\mathbf{u}_{\mathrm{D},m}), \mathrm{acos}(\mathbf{r}_{\mathrm{BS},3}^{\mathsf{T}}\mathbf{u}_{\mathrm{D},m})]^{\mathsf{T}}.$$

D. Derivatives With Respect to UE Rotation Matrix

We make use of (46a), (46c), and (46d),

$$\frac{\partial \theta_{\mathrm{A},m}^{(\mathrm{el})}}{\partial \mathbf{R}_{\mathrm{UE}}} = -\frac{\mathbf{u}_{\mathrm{A},m}\mathbf{u}_3^{\mathsf{T}}}{\sqrt{1-(\mathbf{r}_{\mathrm{UE},3}^{\mathsf{T}}\mathbf{u}_{\mathrm{A},m})^2}}, \tag{48a}$$

$$\frac{\partial \theta_{\mathrm{A},m}^{(\mathrm{az})}}{\partial \mathbf{R}_{\mathrm{UE}}} = \frac{(\mathbf{r}_{\mathrm{UE},1}^{\mathsf{T}}\mathbf{u}_{\mathrm{A},m})\mathbf{u}_{\mathrm{A},m}\mathbf{u}_2^{\mathsf{T}} - (\mathbf{r}_{\mathrm{UE},2}^{\mathsf{T}}\mathbf{u}_{\mathrm{A},m})\mathbf{u}_{\mathrm{A},m}\mathbf{u}_1^{\mathsf{T}}}{(\mathbf{r}_{\mathrm{UE},1}^{\mathsf{T}}\mathbf{u}_{\mathrm{A},m})^2 + (\mathbf{r}_{\mathrm{UE},2}^{\mathsf{T}}\mathbf{u}_{\mathrm{A},m})^2}. \tag{48b}$$

Note that AoDs and ToAs have no dependence on $\mathbf{R}_{\mathrm{UE}}$, leading to partial derivative $\mathbf{0}_{3\times 3}$.

E. Derivatives With Respect to UE Position

The derivatives with respect to $\mathbf{p}_{\mathrm{UE}}$ are obtained using the chain rule. We make use of (46b), (46c) and (46d) to obtain

$$\frac{\partial \theta_{\mathrm{A},m}^{(\mathrm{el})}}{\partial \mathbf{u}_{\mathrm{A},m}} = -\frac{\mathbf{r}_{\mathrm{UE},3}}{\sqrt{1-(\mathbf{r}_{\mathrm{UE},3}^{\mathsf{T}}\mathbf{u}_{\mathrm{A},m})^2}}, \tag{49a}$$

$$\frac{\partial \theta_{\mathrm{A},m}^{(\mathrm{az})}}{\partial \mathbf{u}_{\mathrm{A},m}} = \frac{(\mathbf{r}_{\mathrm{UE},1}^{\mathsf{T}}\mathbf{u}_{\mathrm{A},m})\mathbf{r}_{\mathrm{UE},2} - (\mathbf{r}_{\mathrm{UE},2}^{\mathsf{T}}\mathbf{u}_{\mathrm{A},m})\mathbf{r}_{\mathrm{UE},1}}{(\mathbf{r}_{\mathrm{UE},1}^{\mathsf{T}}\mathbf{u}_{\mathrm{A},m})^2 + (\mathbf{r}_{\mathrm{UE},2}^{\mathsf{T}}\mathbf{u}_{\mathrm{A},m})^2}, \tag{49b}$$

$$\frac{\partial \theta_{\mathrm{D},m}^{(\mathrm{el})}}{\partial \mathbf{u}_{\mathrm{D},m}} = -\frac{\mathbf{r}_{\mathrm{BS},3}}{\sqrt{1-(\mathbf{r}_{\mathrm{BS},3}^{\mathsf{T}}\mathbf{u}_{\mathrm{D},m})^2}}, \tag{49c}$$

$$\frac{\partial \theta_{\mathrm{D},m}^{(\mathrm{az})}}{\partial \mathbf{u}_{\mathrm{D},m}} = \frac{(\mathbf{r}_{\mathrm{BS},1}^{\mathsf{T}}\mathbf{u}_{\mathrm{D},m})\mathbf{r}_{\mathrm{BS},2} - (\mathbf{r}_{\mathrm{BS},2}^{\mathsf{T}}\mathbf{u}_{\mathrm{D},m})\mathbf{r}_{\mathrm{BS},1}}{(\mathbf{r}_{\mathrm{BS},1}^{\mathsf{T}}\mathbf{u}_{\mathrm{D},m})^2 + (\mathbf{r}_{\mathrm{BS},2}^{\mathsf{T}}\mathbf{u}_{\mathrm{D},m})^2}, \tag{49d}$$

and (46e) to obtain

$$\partial \mathbf{u}_{\mathrm{A},m\neq 0}/\partial \mathbf{p}_{\mathrm{UE}} = \left(\mathbf{u}_{\mathrm{A},m}\mathbf{u}_{\mathrm{A},m}^{\mathsf{T}} - \mathbf{I}_3\right)/\|\mathbf{p}_m - \mathbf{p}_{\mathrm{UE}}\|, \tag{50a}$$

$$\partial \mathbf{u}_{\mathrm{A},0}/\partial \mathbf{p}_{\mathrm{UE}} = \left(\mathbf{u}_{\mathrm{A},0}\mathbf{u}_{\mathrm{A},0}^{\mathsf{T}} - \mathbf{I}_3\right)/\|\mathbf{p}_{\mathrm{BS}} - \mathbf{p}_{\mathrm{UE}}\|, \tag{50b}$$

$$\partial \mathbf{u}_{\mathrm{D},0}/\partial \mathbf{p}_{\mathrm{UE}} = \left(\mathbf{I}_3 - \mathbf{u}_{\mathrm{D},0}\mathbf{u}_{\mathrm{D},0}^{\mathsf{T}}\right)/\|\mathbf{p}_{\mathrm{UE}} - \mathbf{p}_{\mathrm{BS}}\|, \tag{50c}$$

and $\partial \mathbf{u}_{\mathrm{D},m\neq 0}/\partial \mathbf{p}_{\mathrm{UE}} = \mathbf{0}_{3\times 3}$. Also, considering (46f) gives

$$\frac{\partial \tau_m}{\partial \mathbf{p}_{\mathrm{UE}}} = \begin{cases} (\mathbf{p}_{\mathrm{UE}} - \mathbf{p}_{\mathrm{BS}})/(c\,\|\mathbf{p}_{\mathrm{UE}} - \mathbf{p}_{\mathrm{BS}}\|) & m = 0 \\ (\mathbf{p}_{\mathrm{UE}} - \mathbf{p}_m)/(c\,\|\mathbf{p}_{\mathrm{UE}} - \mathbf{p}_m\|) & m \neq 0 \end{cases}. \tag{51}$$

F. Derivatives With Respect to Incidence Points Positions

The derivatives with respect to IP positions are also obtained using the chain rule. We note that $\partial \mathbf{u}_{\mathrm{A},m}/\partial \mathbf{p}_n = \mathbf{0}_3$, $n \neq m$, for $m = 0, \ldots, M$ and $n = 1, \ldots, M$, with the same case for $\partial \mathbf{u}_{\mathrm{A},m}/\partial \mathbf{p}_n$ and $\partial \tau_m/\partial \mathbf{p}_n$, while for $m \neq 0$

$$\partial \mathbf{u}_{\mathrm{A},m}/\partial \mathbf{p}_m = \left(\mathbf{I}_3 - \mathbf{u}_{\mathrm{A},m}\mathbf{u}_{\mathrm{A},m}^{\mathsf{T}}\right)/\|\mathbf{p}_m - \mathbf{p}_{\mathrm{UE}}\|, \tag{52a}$$

$$\partial \mathbf{u}_{\mathrm{D},m}/\partial \mathbf{p}_m = \left(\mathbf{I}_3 - \mathbf{u}_{\mathrm{D},m}\mathbf{u}_{\mathrm{D},m}^{\mathsf{T}}\right)/\|\mathbf{p}_m - \mathbf{p}_{\mathrm{BS}}\| \tag{52b}$$

$$\partial \tau_m/\partial \mathbf{p}_m = (\mathbf{p}_m - \mathbf{p}_{\mathrm{BS}})/(c\,\|\mathbf{p}_m - \mathbf{p}_{\mathrm{BS}}\|) + (\mathbf{p}_m - \mathbf{p}_{\mathrm{UE}})/(c\,\|\mathbf{p}_m - \mathbf{p}_{\mathrm{UE}}\|). \tag{52c}$$

G. Derivatives With Respect to Clock Bias

The angles have no dependence on b, while $\partial \tau_m/\partial b = 1$.

Appendix B
Solving the Optimization Problem for the Shortest Distance Between Half-Lines

For the half-lines $\ell_1 = \{\mathbf{p} \in \mathbb{R}^3 : \mathbf{p} = \mathbf{p}_1 + t_1\mathbf{d}_1, t_1 \geq 0\}$ and $\ell_2 = \{\mathbf{p} \in \mathbb{R}^3 : \mathbf{p} = \mathbf{p}_2 + t_2\mathbf{d}_2, t_2 \geq 0\}$, the shortest distance $\delta_{\min}$ is obtained from $\delta_{\min}^2 = \min_{\boldsymbol{t}=[t_1,t_2]^{\mathsf{T}}} \|(\mathbf{p}_1 + t_1\mathbf{d}_1) - (\mathbf{p}_2 + t_2\mathbf{d}_2)\|^2$, s.t. $\boldsymbol{t} \geq \mathbf{0}_2$, which is a quadratic convex optimization problem in $\boldsymbol{t}$, and its solution is found by writing the K.K.T. conditions [59]. We utilize a simpler procedure in which we first obtain the unconstrained optimal solution

$$t_1^* = -\mathbf{d}_1^{\mathsf{T}}\left(\mathbf{I} - \mathbf{d}_2\mathbf{d}_2^{\mathsf{T}}\right)\mathbf{p}_{12}/\left(1 - (\mathbf{d}_1^{\mathsf{T}}\mathbf{d}_2)^2\right), \tag{53a}$$

$$t_2^* = \mathbf{d}_2^{\mathsf{T}}\left(\mathbf{I} - \mathbf{d}_1\mathbf{d}_1^{\mathsf{T}}\right)\mathbf{p}_{12}/\left(1 - (\mathbf{d}_1^{\mathsf{T}}\mathbf{d}_2)^2\right), \tag{53b}$$

with $\mathbf{p}_{12} \triangleq \mathbf{p}_1 - \mathbf{p}_2$. If $\boldsymbol{t}^* > \mathbf{0}_2$, the solution is $\delta_{\min} = |\mathbf{n}^{\mathsf{T}}\mathbf{p}_{12}|$ where $\mathbf{n} = (\mathbf{d}_1 \times \mathbf{d}_2)/(\|\mathbf{d}_1 \times \mathbf{d}_2\|)$.

Proof: Substituting the optimal solution (53) in $\|(\mathbf{p}_1 + t_1\mathbf{d}_1) - (\mathbf{p}_2 + t_2\mathbf{d}_2)\|$ gives $\delta_{\min} = \|\mathbf{P}_{\perp}(\mathbf{D}) \cdot \mathbf{p}_{12}\|$, where $\mathbf{D} \triangleq [\mathbf{d}_1, \mathbf{d}_2]$, and $\mathbf{P}_{\perp}(\mathbf{D}) \triangleq \mathbf{I} - \mathbf{D}(\mathbf{D}^{\mathsf{T}}\mathbf{D})^{-1}\mathbf{D}^{\mathsf{T}} = \mathbf{I} - (\mathbf{d}_1\mathbf{d}_1^{\mathsf{T}}(\mathbf{I} - \mathbf{d}_2\mathbf{d}_2^{\mathsf{T}}) + \mathbf{d}_2\mathbf{d}_2^{\mathsf{T}}(\mathbf{I} - \mathbf{d}_1\mathbf{d}_1^{\mathsf{T}}))/(1 - (\mathbf{d}_1^{\mathsf{T}}\mathbf{d}_2)^2)$ is the projector onto the subspace orthogonal to the one spanned by $\mathbf{d}_1$ and $\mathbf{d}_2$, which is in turn spanned by the unit-norm vector $\mathbf{n}$ normal to $\mathbf{d}_1$ and $\mathbf{d}_2$, given by $\mathbf{n} = (\mathbf{d}_1 \times \mathbf{d}_2)/(\|\mathbf{d}_1 \times \mathbf{d}_2\|)$. Hence, $\delta_{\min} = \|(\mathbf{n}^{\mathsf{T}}\mathbf{p}_{12})\,\mathbf{n}\| = |\mathbf{n}^{\mathsf{T}}\mathbf{p}_{12}|$. □

Otherwise, we obtain $\check{t}_1 = -\mathbf{d}_1^{\mathsf{T}}\mathbf{p}_{12}$, $\check{t}_2 = \mathbf{d}_2^{\mathsf{T}}\mathbf{p}_{12}$, $\check{\lambda}_1 = \mathbf{d}_1^{\mathsf{T}}\mathbf{P}_{\perp}(\mathbf{d}_2)\mathbf{p}_{12}$, and $\check{\lambda}_2 = -\mathbf{d}_2^{\mathsf{T}}\mathbf{P}_{\perp}(\mathbf{d}_1)\mathbf{p}_{12}$, where $\mathbf{P}_{\perp}(\mathbf{d}) \triangleq \mathbf{I} - \mathbf{d}\mathbf{d}^{\mathsf{T}}$. If $[\check{t}_1, \check{\lambda}_2]^{\mathsf{T}} > \mathbf{0}_2$, then $\delta_{\min} = \check{\delta}_1$, and if $[\check{t}_2, \check{\lambda}_1]^{\mathsf{T}} > \mathbf{0}_2$, then $\delta_{\min} = \check{\delta}_2$, where $\check{\delta}_1 \triangleq (\mathbf{p}_{12}^{\mathsf{T}}\mathbf{P}_{\perp}(\mathbf{d}_1)\mathbf{p}_{12})^{1/2}$ and $\check{\delta}_2 \triangleq (\mathbf{p}_{12}^{\mathsf{T}}\mathbf{P}_{\perp}(\mathbf{d}_1)\mathbf{p}_{12})^{1/2}$ are both non-negative, due to the Cauchy–Schwarz inequality. Otherwise, $\delta_{\min} = \|\mathbf{p}_{12}\|$. Obtaining expressions is straightforward. As the unconstrained solution $\boldsymbol{t}^*$ often satisfies the constraints, especially in high SNR regimes, this approach is more efficient.

Appendix C
Proof of the Closed-From Expression for the Closest Point to Skew Lines

We determine $\mathbf{p}_0$ to be mutually closest to the half-lines $\ell_1 = \{\mathbf{p} \in \mathbb{R}^3 : \mathbf{p} = \mathbf{p}_1 + t_1\mathbf{d}_1, t_1 \geq 0\}$ and $\ell_2 = \{\mathbf{p} \in \mathbb{R}^3 : \mathbf{p} = \mathbf{p}_2 + t_2\mathbf{d}_2, t_2 \geq 0\}$, in a least-squares sense, so that $\mathrm{d}^2(\mathbf{p}_0, \ell_1) + \mathrm{d}^2(\mathbf{p}_0, \ell_2)$, with $\mathrm{d}(\mathbf{p}_0, \ell_i)$ denoting the distance of $\mathbf{p}_0$ to ℓ_i, $i = 1, 2$, is minimized. According to Pythagorean theorem, $\mathrm{d}^2(\mathbf{p}_0, \ell_i) = \|\mathbf{p}_0 - \mathbf{p}_i\|^2 - ((\mathbf{p}_0 - \mathbf{p}_i)^{\mathsf{T}}\mathbf{d}_i)^2$, where

$(\mathbf{p}_0 - \mathbf{p}_i)^\mathsf{T}\mathbf{d}_i$ is the projection of $(\mathbf{p}_0 - \mathbf{p}_i)$ on line ℓ_i. Taking gradient of $\mathrm{d}^2(\mathbf{p}_0, \ell_1) + \mathrm{d}^2(\mathbf{p}_0, \ell_2)$ with respect to $\mathbf{p}_0$ and setting it to $\mathbf{0}$ results in $\mathbf{p}_0 = \mathbf{A}^{-1}\mathbf{b}$, where $\mathbf{A} = (\mathbf{I} - \mathbf{d}_1\mathbf{d}_1^\mathsf{T}) + (\mathbf{I} - \mathbf{d}_2\mathbf{d}_2^\mathsf{T})$ and $\mathbf{b} = (\mathbf{I} - \mathbf{d}_1\mathbf{d}_1^\mathsf{T})\mathbf{p}_1 + (\mathbf{I} - \mathbf{d}_2\mathbf{d}_2^\mathsf{T})\mathbf{p}_2$. Setting $\mathbf{p}_1 = \mathbf{p}_{\mathrm{BS}}$, $\mathbf{p}_2 = \mathbf{p}_{\mathrm{UE}}(1)$, $\mathbf{d}_1 = \mathbf{R}_{\mathrm{BS}}\mathbf{d}_{\mathrm{D},m}$, and $\mathbf{d}_2 = \hat{\mathbf{R}}_{\mathrm{UE}}\mathbf{d}_{\mathrm{A},m}$ gives (26).

REFERENCES

[1] T. S. Rappaport et al., "Millimeter wave mobile communications for 5G cellular: It will work!," *IEEE Access*, vol. 1, pp. 335–349, 2013.

[2] W. Roh et al., "Millimeter-wave beamforming as an enabling technology for 5G cellular communications: Theoretical feasibility and prototype results," *IEEE Commun. Mag.*, vol. 52, no. 2, pp. 106–113, Feb. 2014.

[3] R. Di Taranto, S. Muppirisetty, R. Raulefs, D. Slock, T. Svensson, and H. Wymeersch, "Location-aware communications for 5G networks: How location information can improve scalability, latency, and robustness of 5G," *IEEE Signal Process. Mag.*, vol. 31, no. 6, pp. 102–112, Nov. 2014.

[4] A. Alammouri, J. Mo, B. L. Ng, J. C. Zhang, and J. G. Andrews, "Hand grip impact on 5G mmWave mobile devices," *IEEE Access*, vol. 7, pp. 60532–60544, 2019.

[5] A. Shastri et al., "A review of millimeter wave device-based localization and device-free sensing technologies and applications," *IEEE Commun. Surv. Tut.*, vol. 24, no. 3, pp. 1708–1749, Thirdquarter 2022.

[6] S. Thrun, "Probabilistic robotics," *Commun. ACM*, vol. 45, no. 3, pp. 52–57, 2002.

[7] S. Bartoletti et al., "Positioning and sensing for vehicular safety applications in 5G and beyond," *IEEE Commun. Mag.*, vol. 59, no. 11, pp. 15–21, Nov. 2021.

[8] K. Witrisal et al., "High-accuracy localization for assisted living: 5G systems will turn multipath channels from foe to friend," *IEEE Signal Process. Mag.*, vol. 33, no. 2, pp. 59–70, Mar. 2016.

[9] A. Albanese, V. Sciancalepore, and X. Costa-Pérez, "First responders got wings: UAVs to the rescue of localization operations in beyond 5G systems," *IEEE Commun. Mag.*, vol. 59, no. 11, pp. 28–34, Nov. 2021.

[10] A. Behravan et al., "Positioning and sensing in 6G: Gaps, challenges, and opportunities," *IEEE Veh. Technol. Mag.*, vol. 18, no. 1, pp. 40–48, Mar. 2023.

[11] J. Wahlström, I. Skog, and P. Händel, "Smartphone-based vehicle telematics: A ten-year anniversary," *IEEE Trans. Intell. Transp. Syst.*, vol. 18, no. 10, pp. 2802–2825, Oct. 2017.

[12] D. Dardari, P. Closas, and P. M. Djurić, "Indoor tracking: Theory, methods, and technologies," *IEEE Trans. Veh. Technol.*, vol. 64, no. 4, pp. 1263–1278, Apr. 2015.

[13] J. A. del Peral-Rosado, R. Raulefs, J. A. López-Salcedo, and G. Seco-Granados, "Survey of cellular mobile radio localization methods: From 1G to 5G," *IEEE Commun. Surv. Tut.*, vol. 20, no. 2, pp. 1124–1148, Secondquarterxs 2018.

[14] 3rd Generation Partnership Project (3GPP), "Study on NR positioning support," 3GPP, Sophia Antipolis, France, Tech Rep. 38.855 16.0.0, 2019.

[15] S. Dwivedi et al., "Positioning in 5G networks," *IEEE Commun. Mag.*, vol. 59, no. 11, pp. 38–44, Nov. 2021.

[16] Z. Abu-Shaban, X. Zhou, T. Abhayapala, G. Seco-Granados, and H. Wymeersch, "Error bounds for uplink and downlink 3D localization in 5G millimeter wave systems," *IEEE Trans. Wireless Commun.*, vol. 17, no. 8, pp. 4939–4954, Aug. 2018.

[17] E. Björnson et al., "Reconfigurable intelligent surfaces: A signal processing perspective with wireless applications," *IEEE Signal Process. Mag.*, vol. 39, no. 2, pp. 135–158, Mar. 2022.

[18] A. Elzanaty, A. Guerra, F. Guidi, and M.-S. Alouini, "Reconfigurable intelligent surfaces for localization: Position and orientation error bounds," *IEEE Trans. Signal Process.*, vol. 69, pp. 5386–5402, 2021.

[19] N. Garcia, H. Wymeersch, E. G. Larsson, A. M. Haimovich, and M. Coulon, "Direct localization for massive MIMO," *IEEE Trans. Signal Process.*, vol. 65, no. 10, pp. 2475–2487, May 2017.

[20] O. Kanhere and T. S. Rappaport, "Position location for futuristic cellular communications: 5G and beyond," *IEEE Commun. Mag.*, vol. 59, no. 1, pp. 70–75, Jan. 2021.

[21] G. Kwon, A. Conti, H. Park, and M. Z. Win, "Joint communication and localization in millimeter wave networks," *IEEE J. Sel. Topics Signal Process.*, vol. 15, no. 6, pp. 1439–1454, Nov. 2021.

[22] M. A. Nazari, G. Seco-Granados, P. Johannisson, and H. Wymeersch, "3D orientation estimation with multiple 5G mmWave base stations," in *Proc. IEEE Int. Conf. Commun.*, 2021, pp. 1–6, doi: 10.1109/ICC42927.2021.9500778.

[23] Y. Liu, Y. Shen, and M. Z. Win, "Single-anchor localization and synchronization of full-duplex agents," *IEEE Trans. Commun.*, vol. 67, no. 3, pp. 2355–2367, Mar. 2019.

[24] A. Shahmansoori, G. E. Garcia, G. Destino, G. Seco-Granados, and H. Wymeersch, "Position and orientation estimation through millimeter-wave MIMO in 5G systems," *IEEE Trans. Wireless Commun.*, vol. 17, no. 3, pp. 1822–1835, Mar. 2018.

[25] J. Li, M. F. Da Costa, and U. Mitra, "Joint localization and orientation estimation in millimeter-wave MIMO OFDM systems via atomic norm minimization," *IEEE Trans. Signal Process.*, vol. 70, pp. 4252–4264, 2022.

[26] R. Mendrzik, H. Wymeersch, G. Bauch, and Z. Abu-Shaban, "Harnessing NLOS components for position and orientation estimation in 5G millimeter wave MIMO," *IEEE Trans. Wireless Commun.*, vol. 18, no. 1, pp. 93–107, Jan. 2019.

[27] F. Wen and H. Wymeersch, "5G synchronization, positioning, and mapping from diffuse multipath," *IEEE Wireless Commun. Lett.*, vol. 10, no. 1, pp. 43–47, Jan. 2021.

[28] A. Guerra, F. Guidi, and D. Dardari, "Single-anchor localization and orientation performance limits using massive arrays: MIMO vs. beamforming," *IEEE Trans. Wireless Commun.*, vol. 17, no. 8, pp. 5241–5255, Aug. 2018.

[29] A. Kakkavas, M. H. Castañeda García, R. A. Stirling-Gallacher, and J. A. Nossek, "Performance limits of single-anchor millimeter-wave positioning," *IEEE Trans. Wireless Commun.*, vol. 18, no. 11, pp. 5196–5210, Nov. 2019.

[30] B. Sun, B. Tan, W. Wang, and E. S. Lohan, "A comparative study of 3D UE positioning in 5G new radio with a single station," *Sensors*, vol. 21, no. 4, 2021, Art. no. 1178, doi: 1424-8220/21/4/1178.

[31] Y. Chen, J. Palacios, N. González-Prelcic, T. Shimizu, and H. Lu, "Joint initial access and localization in millimeter wave vehicular networks: A hybrid model/data driven approach," in *Proc. IEEE 12th Sensor Array Multichannel Signal Process. Workshop*, 2022, pp. 355–359.

[32] E. Björnson, L. Sanguinetti, H. Wymeersch, J. Hoydis, and T. L. Marzetta, "Massive MIMO is a reality—what is next?: Five promising research directions for antenna arrays," *Digit. Signal Process.*, vol. 94, pp. 3–20, 2019.

[33] S. Shen, S. Li, and H. Steendam, "Simultaneous position and orientation estimation for visible light systems with multiple LEDs and multiple PDs," *IEEE J. Sel. Areas Commun.*, vol. 38, no. 8, pp. 1866–1879, Aug. 2020.

[34] J. Jiang, G. Wang, and K. C. Ho, "Sensor network-based rigid body localization via semi-definite relaxation using arrival time and doppler measurements," *IEEE Trans. Wireless Commun.*, vol. 18, no. 2, pp. 1011–1025, Feb. 2019.

[35] S. P. Chepuri, G. Leus, and A.-J. van der Veen, "Rigid body localization using sensor networks," *IEEE Trans. Signal Process.*, vol. 62, no. 18, pp. 4911–4924, Sep. 2014.

[36] Y. Wang, G. Wang, S. Chen, K. C. Ho, and L. Huang, "An investigation and solution of angle based rigid body localization," *IEEE Trans. Signal Process.*, vol. 68, pp. 5457–5472, 2020.

[37] Z. Li, F. Jiang, H. Wymeersch, and F. Wen, "An iterative 5G positioning and synchronization algorithm in NLOS environments with multi-bounce paths," *IEEE Wireless Commun. Lett.*, 2023.

[38] J. Hong, J. Rodríguez-Piñeiro, X. Yin, and Z. Yu, "Joint channel parameter estimation and scatterers localization," *IEEE Trans. Wireless Commun.*, vol. 22, no. 5, pp. 3324–3340, May 2023.

[39] J.-L. Blanco, "A tutorial on SE(3) transformation parameterizations and on-manifold optimization," 2021. [Online]. Available: https://arxiv.org/abs/2103.15980

[40] C. Huang, L. Liu, C. Yuen, and S. Sun, "Iterative channel estimation using LSE and sparse message passing for mmWave MIMO systems," *IEEE Trans. Signal Process.*, vol. 67, no. 1, pp. 245–259, Jan. 2019.

[41] F. Roemer, M. Haardt, and G. Del Galdo, "Analytical performance assessment of multi-dimensional matrix-and tensor-based ESPRIT-type algorithms," *IEEE Trans. Signal Process.*, vol. 62, no. 10, pp. 2611–2625, May 2014.

[42] F. Bellili, F. Sohrabi, and W. Yu, "Generalized approximate message passing for massive MIMO mmWave channel estimation with Laplacian prior," *IEEE Trans. Commun.*, vol. 67, no. 5, pp. 3205–3219, May 2019.

[43] X. Cheng, C. Tang, and Z. Zhang, "Accurate channel estimation for millimeter-wave MIMO systems," *IEEE Trans. Veh. Technol.*, vol. 68, no. 5, pp. 5159–5163, May 2019.

[44] Z. Zhou, J. Fang, L. Yang, H. Li, Z. Chen, and R. S. Blum, "Low-rank tensor decomposition-aided channel estimation for millimeter wave MIMO-OFDM systems," *IEEE J. Sel. Areas Commun.*, vol. 35, no. 7, pp. 1524–1538, Jul. 2017.

[45] R. Thomä, M. Landmann, and A. Richter, "RIMAX-A maximum likelihood framework for parameter estimation in multidimensional channel sounding," in *Proc. Int. Symp. Antennas Propag.*, 2004, pp. 53–56.

[46] T. E. Abrudan, Z. Xiao, A. Markham, and N. Trigoni, "Underground incrementally deployed magneto-inductive 3-D positioning network," *IEEE Trans. Geosci. Remote Sens.*, vol. 54, no. 8, pp. 4376–4391, Aug. 2016.

[47] H. Wymeersch, J. Lien, and M. Z. Win, "Cooperative localization in wireless networks," *Proc. IEEE*, vol. 97, no. 2, pp. 427–450, Feb. 2009.

[48] M.-A. Badiu, T. L. Hansen, and B. H. Fleury, "Variational Bayesian inference of line spectra," *IEEE Trans. Signal Process.*, vol. 65, no. 9, pp. 2247–2261, May 2017.

[49] K. V. Mardia and P. E. Jupp, *Directional Statistics*, vol. 494. Hoboken, NJ, USA: Wiley, 2009.

[50] N. Boumal, "An introduction to optimization on smooth manifolds," Aug. 2020. [Online]. Available: http://www.nicolasboumal.net/book

[51] S. Wright and J. Nocedal, *Numerical Optimization*, vol. 35. Berlin, Germany: Springer, 1999, pp. 67–68.

[52] J. Vince, *Rotation Transforms for Computer Graphics*. Berlin, Germany: Springer, 2011.

[53] S. M. Kay, *Fundamentals of Statistical Signal Processing: Estimation Theory*. Hoboken, NJ. USA: Prentice-Hall, 1993.

[54] P. Stoica and B. C. Ng, "On the Cramér-Rao bound under parametric constraints," *IEEE Signal Process. Lett.*, vol. 5, no. 7, pp. 177–179, Jul. 1998.

[55] A. S. Rahmathullah, Á. F. García-Fernández, and L. Svensson, "Generalized optimal sub-pattern assignment metric," in *Proc. IEEE 20th Int. Conf. Inf. Fusion*, 2017, pp. 1–8.

[56] C. A. Balanis, *Antenna Theory: Analysis and Design*. Hoboken, NJ, USA: Wiley, 2015.

[57] N. Boumal, B. Mishra, P.-A. Absil, and R. Sepulchre, "Manopt, a Matlab toolbox for optimization on manifolds," *J. Mach. Learn. Res.*, vol. 15, no. 42, pp. 1455–1459, 2014. [Online]. Available: https://www.manopt.org

[58] J. Segura, "Bounds for ratios of modified Bessel functions and associated Tur-type inequalities," *J. Math. Anal. Appl.*, vol. 374, no. 2, pp. 516–528, 2011.

[59] S. Boyd, S. P. Boyd, and L. Vandenberghe, *Convex Optimization*. Cambridge, U.K.: Cambridge Univ. Press, 2004.